

Self-floating g-C₃N₄/h-BN/Au photo-thermal catalysts with unprecedented thermostability at solar-activated heating condition for reusable degradation of organic pollutants

Chang Wang^a, Shihao Zhou^b, Qingqiang Cui^a, Mengya Zhang^a, Linqi Zheng^c, Shuang Li^c, Xiangdong Liu^a, Ming Chen^{a,*}

^a School of Physics and National Demonstration Center for Experimental Physics Education, Shandong University, Shandong, Jinan 250100, PR China

^b Department of Physics and Astronomy, The University of North Carolina at Chapel Hill, NC 27599, USA

^c School of Science, Shandong Jianzhu University, Shandong, Jinan 250101, PR China



ARTICLE INFO

Keywords:

Synergistic PTC decontamination
g-C₃N₄/h-BN/Au heterostructures
Dual-interfacial charge transfer channels
Ultrahigh PTC activity
Unprecedented thermostability

ABSTRACT

Photo-thermal catalytic (PTC) degradation as an ideal candidate for wastewater treatment is yet suffering from the unsatisfied recyclability due to the thermal effect-exacerbated serious photocorrosion of semiconductor-based catalysts. Based on polymeric graphite carbon nitride (g-C₃N₄) hybridized with antioxidative hexagonal boron nitride (h-BN) and grafted with stable Au nanoparticles (NPs), we provide thermostable g-C₃N₄/h-BN/Au nano-catalysts for high-efficient degradation of organic dyes at solar-activated heating condition. The fantastic PTC activity with optimal degradation rate up to ~ 0.30 min⁻¹ is far better than most mainstream hybrid catalysts. The unprecedented thermal recyclability is convincingly verified by consecutive 10 repeated tests within 500 min measurements under solar-driven heating condition (~60 °C), wherein the negligible drop of degradation efficiency is only ~ 0.2% lower than pristine one. The ingenious self-floating PTC membranes can be conveniently established by immobilizing the resultant nano-catalysts into bio-carbon porous frames and viscous bacterial nano-celluloses, facilitating practical wastewater decontamination in real-world scenarios.

1. Introduction

As for the wastewater decontamination by virtue of taking full advantage of renewable solar energy, the imperative photocatalytic degradation has been well-established as a promising green treatment for eliminating diverse artificial poisonous pollutants (organic dyes, antibiotics, hormones and/or inorganic heavy metal contaminants, etc.) [1–6]. Consequently, the development of highly-efficient photocatalysts with remarkable utilization of broadband solar lights becomes the primary goal for enhancing photocatalytic degradation efficiency and then propelling wastewater purification in widespread ecosystems. By introducing metallic, transition-metallic, or nonmetallic cocatalysts, the most popular semiconductor-based photocatalysts are frequently explored to capture and harvest more solar light spectrums, spanning ultraviolet (UV) to visible and then near-infrared (NIR) region. The improved photoredox catalysis for chemical bond breaking reaction is generally attributed to the formation of enriched charge carriers under broadband light irradiation [2,7]. Besides the bare photoredox reaction,

the emerging synergistic photo-thermal catalytic (PTC) system has then aroused extensive attention on account of double contributions originating from both the intrinsic effect of direct photoexcitation and additional utilization of photo-driven thermal energy [5,8–13]. Recently, an interesting Bi₁₂CoO₂₀ selenite with a thermal-induced strong internal electric field under solar wide-spectrum irradiation was reported to provide excellent PTC degradation of aqueous phenols and the degradation rate was ~ 3 times higher than that of commercial P25-TiO₂ [13]. Undoubtedly, it is convincingly revealed that the ingenious PTC degradation with remarkable photo-thermal conversion holds great potential for maximizing the solar energy utilization toward wastewater purification.

Despite the admirable PTC activity through the reutilization of solar-driven thermal energy, nearly all of semiconductor-based photocatalysts developed in previous works are still far from satisfactory for the implementation of PTC degradation from a promising state to practical wastewater treatment. The immense challenge is attributed to the thermal effect-exacerbated serious photocorrosion of most

* Corresponding author.

E-mail address: chenming@sdu.edu.cn (M. Chen).

semiconductor composites at high-temperature condition, creating a huge barrier for sufficiently recyclable and sustainable PTC degradation in long-term application. As is well known, the ubiquitous photo-corrosion of semiconductors under solar light illumination should be mainly derived from the severe accumulation of excess photoexcited holes or electrons on their surfaces [14–16]. Consequently, the gathered charge carriers can participate in the self-oxidation and/or reduction of band-gap semiconductor components, ceaselessly resulting in the inevitable decomposition/collapse of as-prepared microstructures. In this way, the photocorrosion of semiconductor components will not only consume the photo-generated energetic carriers that are used in the photoredox degradation but also cause the obvious deactivation of catalytic sites on the deteriorated surfaces. To effectively mitigate the detrimental photocorrosion and obtain excellent recyclability of photocatalysts, various strategies have been carefully developed till now. They include the modification of crystallinity to diminish the recombination centers [17], controlling hollow or porous structures coupled with metal ions [18], heterojunction construction with built-in electric field [19–21] or doping metallic or carbon-dot (CD) cocatalysts severed as electron/hole acceptors [22–25], etc. These previous efforts have been exclusively devoted to constructing a single effective charge transfer channel in semiconductor composites for boosting the electron-hole separation and accelerating transfer efficiency. However, only one transfer channel formed in each sample merely focuses on either the photogenerated electron capture or the photoexcited hole extraction, while few tackle both issues jointly. In this way, the incomplete separation/transformation of photoinduced electrons and holes will also result in the remaining photocorrosion that is often neglected or largely underestimated in many previous photocatalysts with restricted stability at mere hours [26]. Unfortunately, even the inconspicuous photocorrosion-induced deactivation can be also seriously exacerbated under thermal-heated high temperature conditions [27,28]. Although many desirable semiconductor-based photocatalysts can be reusable in the traditional photocatalytic degradations, most of them are not suitable for the recyclable PTC system at high temperature condition. Therefore, an urgent need exists for the construction of novel structured nano-catalysts that can efficiently address the thermal effect-exacerbated photocorrosion, facilitating PTC commercial viability in environmental remediation.

Superior to the conventional photocatalysts modified with a single charge carrier channel in each sample, the more exquisite-heterostructures by loading dual cocatalysts have a greater ability to significantly promote the spatial separations of photoexcited electrons and holes and then respectively accelerate their transfer efficiencies [29–32]. Consequently, the smart design with dual interfacial charge transfer channels is extremely conducive to the best use of photo-generated carriers when both the separated electrons and holes can be simultaneously and timely utilized for designed photocatalytic redox reactions [33]. Most recently, a bifunctional photocatalyst consisting of CdS/MoO₂/MoS₂ hollow nano-spheres with dual-cocatalysts was established for hydrogen evolution reaction (HER) and pyruvic acid (PA) synthesis [34]. It is expected to provide not only excellent catalytic activity via the formation of abundant energetic carriers but also possess satisfactory photostability due to very little charge accumulation on the heterostructures. Up to now, the promising strategy is still solely restricted to renewable energy systems, yet it is rarely applied to highly recyclable PTC catalysts.

Herein, we report highly efficient and thermostable PTC nano-catalysts through two-dimensional (2D) graphite carbon nitride (g-C₃N₄) nanoplates hybridized with hexagonal boron nitride (h-BN) nanosheets and grafted with dense plasmonic Au nanoparticles (NPs). The competitive merits are highlighted as follows: (I) polymeric layered g-C₃N₄ with low band-gap (~2.7 eV) are more suitable for harvesting broadband light energy and offering plentiful photogenerated energetic carriers [8,35,36]; (II) the stable Au NPs with localized surface plasmon resonance (LSPR) provide hot charge carriers for further elevating PTC

reaction, which is also ideal electron acceptors for extraction of photo-excited electrons from semiconductors [37]; (III) the electronegative h-BN insulators with large band-gap (~5.6 eV) are featured by excellent thermal-chemical stability and antioxidant capacity [38–40], which can be served as effective hole capturers for transferring photoinduced electropositive holes from the dominate g-C₃N₄ catalysts. Due to the dual charge carrier transfer channels established in g-C₃N₄/h-BN/Au NPs, making the best of photoinduced energetic carriers at solar-driven heating conditions (~60 °C) gives rise to the optimal PTC degradation rate as high as ~0.30 min⁻¹ that is far better than many previous works. Importantly, the successful migration of photogenerated holes could also avoid the photocorrosion-induced self-oxidative decomposition of g-C₃N₄ catalysts (2 N³⁻ + 6 h⁺ → N₂) [14,37,41–43] and there are ~99.8% PTC activity can be well maintained after consecutive 10 repeated tests within 500 min measurements at solar-assisted high temperature (~60 °C), confirming the unparalleled long-term thermostability. Finally, the self-floating PTC flexible membranes are then established by grafting the resultant g-C₃N₄/h-BN/Au NPs into 3D bio-carbon porous frames combined with viscous bacterial nano-celluloses (BNCs). The present work provides an admirable robust PTC system for improving wastewater purification.

2. Experimental section

2.1. Materials

Chloroauric acid (HAuCl₄), Polyvinyl pyrrolidone (PVP), ciprofloxacin (CIP), pendimethalin (PDM) and rhodamine 6 G (R6G) molecules were purchased from Aladdin Chemistry Co., Ltd (Shanghai, China). The hexagonal boron nitride (h-BN), L-ascorbic acid (L-AA), ammonium oxalate (AO) and dicyandiamide (C₂H₄N₄) were purchased from Macklin Chemistry Co., Ltd. Isopropyl alcohol (IPA), sodium hydroxide (NaOH), sodium sulfate (Na₂SO₄), sodium dihydrogen phosphate (Na₂HPO₄), disodium hydrogen phosphate (Na₂HPO₄) and were purchased from Sinopharm Chemical Reagent Co. (Shanghai, China). Luffa was purchased from the local farmers market and the bacterial cellulose (BNCs) samples were purchased from Guanlan Technology Limited Corporation. Ethanol (C₂H₅OH) was obtained from Tianjin Fuyu. All chemical reagents were of analytical grade and used as received without further purification in all experiments.

2.2. Preparation of PTC catalysts

2.2.1. Synthesis of hybrid g-C₃N₄/h-BN supports

The hybrid g-C₃N₄/h-BN supports were prepared by a facile calcination strategy. Typically, a certain amount (1.0 g) of C₂H₄N₄ and 2 mg of h-BN were added into an agate mortar and grounded together. The obtained powders were transferred to a covered crucible and then calcined at 550 °C for 3 h with a heating rate of 10 °C/min. For comparison, bulk g-C₃N₄ powders without the addition of h-BN were also similarly prepared by calcination strategy.

2.2.2. Synthesis of g-C₃N₄/h-BN/Au NPs heterostructures

The g-C₃N₄/h-BN/Au NPs heterostructures were fabricated by laser irradiation of g-C₃N₄/h-BN in supports HAuCl₄ solution. The typical steps are as follows: 20 mg of g-C₃N₄/h-BN powders were dispersed in 20 mL water and then ultrasound for about 2 h to form a uniformly dispersed colloidal solution. Then, 5 mL g-C₃N₄/h-BN suspensions were diluted into 5 mL DI water by ultrasonic treatment to form evenly colloid suspensions, which were then added to 1 mL of ethanol with 100 μL HAuCl₄ (0.05 M). For comparison, the g-C₃N₄/h-BN/Au NPs with different metallic compositions were obtained by changing the amount of HAuCl₄ (0.01 mM, 0.02 mM, 0.1 mM, 1 mM). The different mixtures were separately irradiated by a continuous 405 nm laser beam with a power of ~345 mW and an average diameter of 2 cm. After irradiation of 60 min, the suspensions were centrifuged and washed with DI water

three times. The g-C₃N₄/h-BN/Au nanocomposites were obtained by keeping them at 60 °C overnight in the drying oven. The obtained precipitates were washed with DI water three times and then dried at 60 °C overnight. For comparison, h-BN/Au NPs and g-C₃N₄/Au NPs were also prepared in this work.

2.3. Synthesis of biomimetic PTC film

Preparation of Bio-Carbon: The loofah was collected from the local farmers market, cut into small pieces, washed with tap water three times, and then dried naturally. The air-dried loofah was packed into a ceramic pot and covered with a lid, then pyrolyzed at 400 °C in a tube furnace for 2 h under an oxygen-limited atmosphere for 6 h to prevent calcination of the biomass in the presence of oxygen. Finally, the loofah was ground into powders.

Preparation of PTC film: Hydrogel bacterial cellulose (BNCs) was smashed into homogenate (10 mg/mL), and 10 mL of BNCs homogenate was mixed with 30 mg carbonized loofah powder. After adding 50 mL g-C₃N₄/h-BN/Au NPs (1 mg/mL), the mixture was sonicated for 10 min and vacuum-filtrated to prepare a free-standing membrane.

2.4. Characterizations

The microscopic morphologies were examined by transmission electron microscopy (TEM) equipped with an energy dispersive X-ray (EDS) spectroscopy via a scanning transmission electron microscopy (STEM) unit (JEOL, JEM-2100 F). The actual compositions of Au and h-BN on the g-C₃N₄ nanosheets were determined by PerkinElmer NexION 300X inductively coupled plasma-mass spectrometry (ICP-MS). The scanning electron microscope (SEM) images and chemical compositions were further characterized by a Focused Ion beam (FIB, Helios G4 UC) equipped with energy-dispersive X-ray spectroscopy (EDS). The crystal structures of as-prepared nano-products were acquired by X-ray diffraction (XRD) patterns (Rigaku, Smart Lab 9 kW) using Cu K α radiation ($\lambda = 0.15406$ nm) in the range of 10–80°. The surface compositions and element valence information were obtained from X-ray photoelectron spectra (XPS) by PHI Quantera SXM. In order to characterize the work function values of different samples, ultraviolet photoelectron spectroscopy (UPS) was collected by PHI5000 VersaProbe III. The absorption spectra were obtained by UV-visible-IR spectrums (UV-1800, Shimadzu) and photoluminescence (PL) spectra were recorded by Hitachi F-4500. The time-resolved fluorescence decay spectra were performed on (FLS920) photo spectrometer (Edinburgh Instruments, Edinburgh, Britain). All of the Raman spectra were collected by using the excitation wavelength 633 nm laser (Renishaw Raman spectroscopy, Britain). The specific surface areas of the nano-catalysts were determined by the Quantachrome Quadrasorb SI porosimeter. The total organic carbon (TOC) results were measured by the organic carbon analyzer in the reaction solution (TOC-L CPH, Shimadzu, Japan). The chemical oxygen demand (COD) was estimated by COD ampoules (HACH Chemical) using a spectrophotometer (DR 600, HACA, USA). Liquid chromatography-mass spectrometer (LC-MS, Agilent 6410, USA) measurements were carried out to determine the main intermediate products during PTC degradation of R6G. Electron spin resonance (ESR, JES-X320) signals of radicals using 5,5-dimethyl-1-pyrroline-N-oxide (DMPO) and 2,2,6,6-Tetramethyl-1-piperidinyloxy (TEMPO) as the capture reagents were recorded to analyze reactive oxygen species. All the photo-electro-chemical measurements were carried out by using the standard three-electrode system with 0.1 M Na₂SO₄ electrolyte solution on a CHI 760E electrochemical workstation (Shanghai Chenhua Instrumental Co., Ltd, China). The photocurrent responses of the photocatalysts as xenon lamp light on or off were measured at 0.0 V and electrochemical impedance spectroscopy (EIS) results were measured with an open-circuit voltage in a frequency range of 0.01–10⁵ Hz with the amplitude of 5 mV. Mott-Schottky plots with frequencies of 1 kHz were collected.

2.5. PTC degradation experiments

The PTC performances of different nano-catalysts were evaluated in terms of the degradation of 10 mg/L R6G dye molecules under xenon lamp irradiation (300 W Xe lamp, Beijing Perfectlight Technology Co., Ltd. equipped with a UV cutoff filter $\lambda > 420$ nm). The solutions with 0.2 M Na₂HPO₄ and 0.2 M NaH₂PO₄ as well as 1 M NaOH were used for preparing buffers in the pH range of 2.2–11.2. After adding different nano-catalysts in this work, the pH value with the negligible deviation < 2% in each of PTC tests has been separately controlled in the prepared buffer solution during degradation experiments. Typically, 5 mg of the prepared photocatalysts powder was dispersed in a 50 mL buffer solution with 10 mg/L R6G dyes. Then the suspension was stirred for 30 min in the dark to ensure the adsorption/desorption equilibrium of organic contaminant before visible-light irradiation. At the given time interval, 2 mL reaction solution was collected and centrifuged to remove the photocatalyst for analysis. The concentration of R6G was measured with a UV-visible-IR spectrometer (Shimadzu, UV-1800). Moreover, the independently prepared 5 samples have been separately adopted in each PTC degradation experiment, in order to repeat their statistical analysis. For recyclable tests, the PTC degradations were examined by every 50 min and repeated 10 times. Finally, the PTC film was extended to the effective degradations in actual water samples.

2.6. Theoretical calculation method

All the calculations are performed in the framework of the density functional theory with the projector-augmented plane-wave method, as implemented in the Vienna ab initio simulation package [44]. The generalized gradient approximation proposed by Perdew-Burke-Ernzerhof (PBE) is selected for the exchange-correlation potential [45]. The cut-off energy for the plane wave is set to 480 eV. The energy criterion is set to 10⁻⁵ eV in the iterative solution of the Kohn-Sham equation. All the structures are relaxed until the residual forces on the atoms have declined to less than 0.02 eV/Å. To avoid interlaminar interactions, a vacuum spacing of 20 Å is applied perpendicular to the slab. The adsorption energy E_{ads} is expressed as.

$$\Delta E_{ads} = E_{A+B} - E_A - E_B \quad (1)$$

where E_{A+B} is the total energy of slab A model with molecule B adsorption, E_A is the energy of a A slab, and E_B is that for a B molecule.

Here, we define $\Delta\rho = \rho_{A+B} - \rho_A - \rho_B$ as the charge density difference of A/B heterostructure, where ρ_{A+B} , ρ_A and ρ_B are the charge densities of A/B heterostructure, isolated A and B slabs, respectively.

3. Results and discussions

3.1. Physical characteristics

The morphologies of the initial g-C₃N₄ and h-BN precursors were first investigated by TEM and high-resolution TEM (HRTEM) measurements (Fig. S1). The TEM images display some scroll-like profiles at the edge regions of polymeric layered nanoplates with 0.33 nm lattice-spacing distance corresponding to (002) plane of initial g-C₃N₄ (Fig. S1(a-b)) and smooth flakiness-shaped nanosheets with 0.32 nm lattice fringes regarded as (002) plane of h-BN crystals (Fig. S1(c-d)), respectively. After thermal annealing treatment, the microstructure of hybrid g-C₃N₄/h-BN supports is illustrated in Fig. 1(a), wherein the two components are already aggregated and stacked together, offering the larger 2D platforms for subsequent overgrowth of plasmonic Au NPs. The high-resolution TEM (HRTEM) image displays a typical interconnected cross region between g-C₃N₄ and h-BN components (Fig. 1(b)), confirming the hinge-jointed structures instead of a simple physical mixture of two individual precursors. The measured lattice-spacing distances in HRTEM images (Fig. 1(c-d)) correspond to the two (002) planes of g-

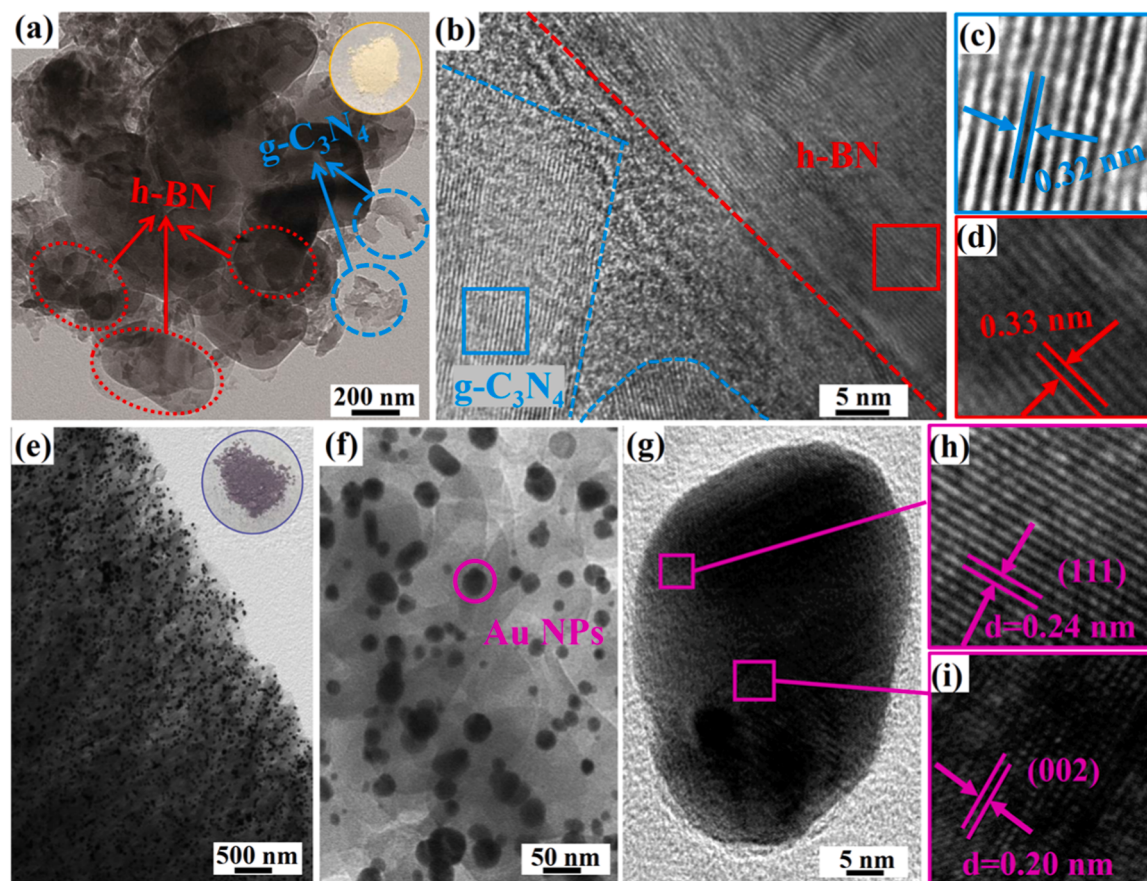


Fig. 1. (a) The typical TEM image of hybrid $\text{g-C}_3\text{N}_4/\text{h-BN}$ supports generated by thermal annealing treatment at 550 °C for 3 h. The inset shows a photograph of the powders. (b-d) The HRTEM of as-prepared $\text{g-C}_3\text{N}_4/\text{h-BN}$ supports. (e-f) The low-magnification TEM image of the obtained $\text{g-C}_3\text{N}_4/\text{h-BN}/\text{Au}$ NPs and the inset demonstrates a photograph of the nano-products, (g-i) the HRTEM image of plasmonic Au NPs loaded on $\text{g-C}_3\text{N}_4/\text{h-BN}$ supports.

C_3N_4 and h-BN components, respectively. Based on the as-prepared 2D $\text{g-C}_3\text{N}_4/\text{h-BN}$ platforms, the ternary $\text{g-C}_3\text{N}_4/\text{h-BN}/\text{Au}$ NPs were generated by photochemical overgrowth of metallic crystals on the lamellar-form nano-supports. As illustrated in Fig. 1(e) and Fig. S2, the highly dense and dispersed metallic NPs with abundant dark-like spots in TEM images are convincingly formed on 2D $\text{g-C}_3\text{N}_4/\text{h-BN}$ platforms by UV laser-induced photoreaction at enough irradiation time (60 min). The color of the powders is also changed from pale yellow (inset in Fig. 1(a)) to brownness (inset in Fig. 1(e)). The enlarged TEM and HRTEM results (Fig. 1(e-f) and Fig. 1(g-i)) demonstrate the successful overgrowth of metallic Au NPs on hybrid $\text{g-C}_3\text{N}_4/\text{h-BN}$ supports, and the crystal fringes of 0.24 nm and 0.20 nm are consistent with (111) and (200) planes in Au face-centered cubic (fcc) crystal structures. By measuring the diameters of more than 500 NPs in sight on the SEM image (Fig. S3(a)), the size distribution histogram of metallic Au NP formed on 2D supports reveals that the average size is mainly centered at ~20 nm (Fig. S3(b)). Moreover, the corresponding EDS pattern of the resultant $\text{g-C}_3\text{N}_4/\text{h-BN}/\text{Au}$ NPs (Fig. S3(c)) reveals that the relative weight ratio of Au component is about 21.8% in the nanocomposites, which is consistent with the result (21.7%) obtained by the inductively coupled plasma mass spectrometry (ICP). The elemental mapping images of a typical part from the $\text{g-C}_3\text{N}_4/\text{h-BN}/\text{Au}$ NPs (Fig. S3(d)) further confirm the dispersed distribution of metallic Au NPs and uniform distribution of nonmetallic C, N and B elements in the nanocomposites. The above experimental results intuitively verify the successful construction of ternary $\text{g-C}_3\text{N}_4/\text{h-BN}/\text{Au}$ NPs by thermal annealing of 2D/2D precursors and then photochemical overgrowth of plasmonic NPs. The mechanism of loading metallic NPs on semiconductor supports is highly attributed to the photoexcitation of electron-hole pairs on band-gap structures and the excited electrons give

rise to the effective reduction of metallic ions, facilitating the subsequent nucleation of metallic atoms [46–50]. Difference from our previous studies with one semiconductor support in each experiment [46–50], there are two sequential steps for the overgrowth of metallic Au NPs on the hybrid 2D $\text{g-C}_3\text{N}_4/\text{h-BN}$ in this work. In detail, the nucleation of Au NPs was preferentially performed on the $\text{g-C}_3\text{N}_4$ nanoplates and then subsequently loaded on the h-BN nanosheets, owing to the different band-gap structures of the two components. When the insufficient illumination time (30 min) was used in photochemical synthesis, nearly all metallic Au NPs were solely loaded on $\text{g-C}_3\text{N}_4$ supports and very few metallic crystals can be detected on 2D h-BN (Fig. S4), even the added reactive HAuCl_4 content was changed from low concentration to high condition. It is mainly attributed to the fact that the band gap of polymeric layered $\text{g-C}_3\text{N}_4$ is lower than the inherent large band gap of 2D h-BN components [38–40], giving rise to the formation of more photo-excited electrons for efficient metallic nucleation. On the other hand, the longer or shorter laser wavelengths, such as 532 nm and 375 nm adopted in this work, would also result in the scattered few Au NPs (Fig. S5(a)) and large-sized metallic agglomerates (Fig. S5(b)), respectively. Therefore, the formation of dense and dispersed Au NPs on the whole 2D $\text{g-C}_3\text{N}_4/\text{h-BN}$ supports in this work is mainly determined by enough irradiation time (60 min) and moderate (405 nm) incident laser wavelength.

Then, a series of experimental tests were carefully carried out to evaluate the physical characteristics of the obtained $\text{g-C}_3\text{N}_4/\text{h-BN}/\text{Au}$ NPs and five references including initial $\text{g-C}_3\text{N}_4$, pristine h-BN, hybrid $\text{g-C}_3\text{N}_4/\text{h-BN}$ supports, binary h-BN/Au NPs and $\text{g-C}_3\text{N}_4/\text{Au}$ NPs (TEM images of two binary samples shown in Fig. S6). The XRD analyses of the above six samples (Fig. 2(a)) reveal the crystal changes during the

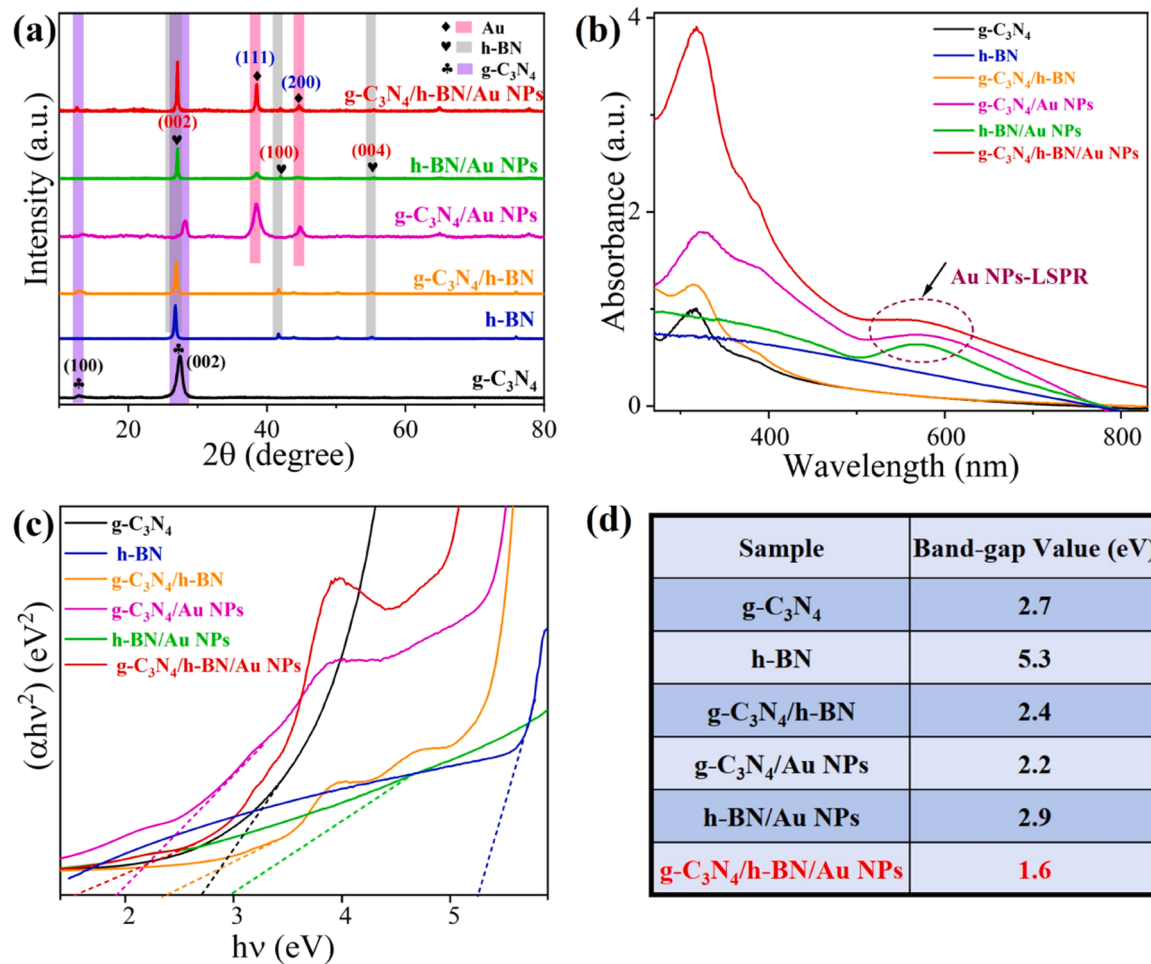


Fig. 2. (a) XRD patterns of the obtained g-C₃N₄/h-BN/Au NPs and reference samples (initial g-C₃N₄ and h-BN, hybrid g-C₃N₄/h-BN, binary h-BN/Au NPs and g-C₃N₄/Au NPs), (b-c) UV-visible absorption spectra and the corresponding Tauc plots of six samples, (d) the estimated band-gap energies of the above samples.

hybridization procedure and then the photochemical overgrowth process. As for g-C₃N₄ nanoplates (black cure in Fig. 2(a)), the two diffraction peaks at about 13.2° and 27.4° are attributed to the (100) and (002) lattice planes (JCPDS No. 87-1526). After hybridizing with h-BN nanosheets, the as-prepared g-C₃N₄/h-BN supports exhibit two additional weak diffraction peaks at about 41.9° and 55.2° that are related to the (101) and (004) planes of h-BN component (JCPDS. No 73-2095). When the metallic Au NPs were loaded on g-C₃N₄ or h-BN precursors, the other diffraction peaks at ~ 38.5° and 44.5° corresponding to (111) and (200) planes of metallic Au crystals are detected on the binary g-C₃N₄/Au NPs or h-BN/Au NPs. Notably, the resultant g-C₃N₄/h-BN/Au NPs possess the characteristic XRD diffraction peaks originating from both two 2D supports and metallic NPs, so the co-existence feature supports the successful formation of ternary compounds. Subsequently, in order to reveal the absorption capacity and band-gap structure of the above six samples, the UV-visible absorption spectra are displayed in Fig. 2(b). It can be found that the original g-C₃N₄ nanoplates exhibit an absorption edge at the visible region, revealing the narrow band-gap structure of the semiconductor. Meanwhile, the absorbance capacity in the visible region (400–700 nm) gradually increases when the sample is changed from binary g-C₃N₄/Au NPs or h-BN/Au NPs to the ternary g-C₃N₄/h-BN/Au NPs. The broadband absorption peak at approximately 550 nm should be mainly attributed to the LSPR oscillation of plasmonic Au NPs. Moreover, to evaluate the band-gap energies of semiconductor components in heterostructures, the Tauc plots of the above six samples are then carried out in Fig. 2(c). The estimation of band-gap value is based on the well-defined equation: $\alpha h\nu = A(h\nu - E_g)^{1/2}$ [6,22,24], where

α , ν , E_g and A are the Plank constant, absorption co-efficient, frequency of light, band-gap, and proportionality constant, respectively. Based on the Tauc plots (Fig. 2(c)), the detailed band-gap values of semiconductor components in the above six samples are also displayed in Fig. 2(d). Clearly, the band-gap of the semiconductor component in Fig. 2(c) shows an obvious red-shift with decorating with h-BN and then loading with plasmonic Au NPs, implying a decrease of the band-gap energy on the obtained g-C₃N₄/h-BN/Au NPs. Especially, the band-gap value of the semiconductor component in the obtained g-C₃N₄/h-BN/Au NPs is obviously reduced to ~1.6 eV, which is definitely lower than that of the initial h-BN (5.3 eV), original g-C₃N₄ (2.7 eV) and g-C₃N₄/h-BN support (2.4 eV) as well as binary g-C₃N₄/Au NPs (2.2 eV). It is implied that the resultant g-C₃N₄/h-BN/Au NPs with narrower band-gap have a greater potential for harvesting more photon energy of visible-NIR light and facilitating the formation of abundant photoexcited charge carriers.

The chemical states of the resultant g-C₃N₄/h-BN/Au NPs and reference samples (pristine g-C₃N₄, g-C₃N₄/h-BN, g-C₃N₄/Au NPs and h-BN/Au NPs) were illustrated by XPS measurements. The survey spectra show that the obvious XPS peaks are derived from C, N, B, and Au elements in the prepared targets and some few O species originated from the surrounding air condition (Fig. S7). Then, the high-resolution XPS patterns of C 1 s, N 1 s, B 1 s and Au 4 f displayed in Fig. 3(a-d) reveal the electron interaction between h-BN and g-C₃N₄ as well as metallic Au components. As for the initial g-C₃N₄ (Fig. 3(a)), the double characteristic peaks of C 1 s at about 284.8 and 288.1 eV are related to the sp²-bonded carbon in C-C adventitious hydrocarbon and N-C≡N coordination in the heptazine structure [8,51,52]. After decorating with h-BN or

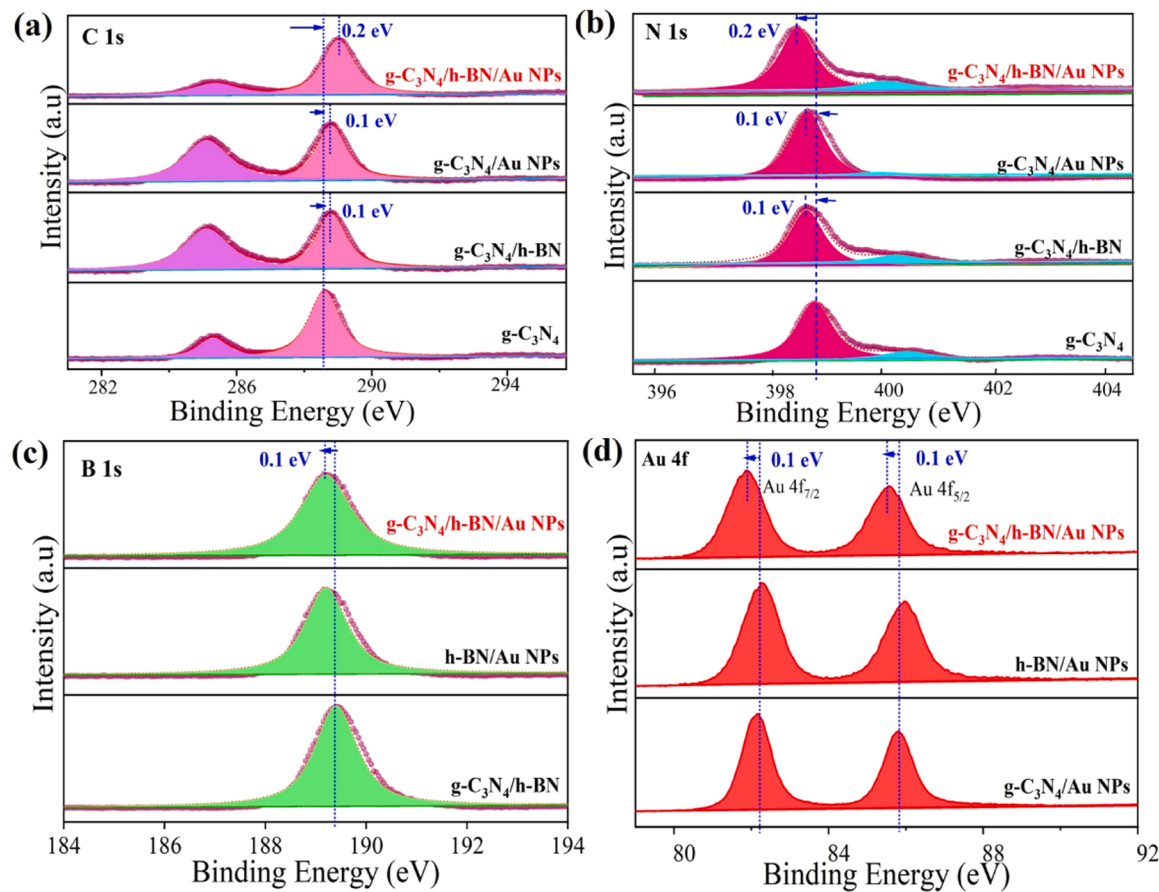


Fig. 3. High-resolution XPS spectra of the resultant $\text{g-C}_3\text{N}_4/\text{h-BN}/\text{Au}$ NPs and reference samples (pristine $\text{g-C}_3\text{N}_4$, hybrid $\text{g-C}_3\text{N}_4/\text{h-BN}$ supports, binary $\text{g-C}_3\text{N}_4/\text{Au}$ NPs and $\text{h-BN}/\text{Au}$ NPs). (a) C 1 s, (b) N 1 s, (c) B 1 s, and (d) Au 4 f.

metallic Au NPs, the XPS peaks of C 1 s originated from $\text{g-C}_3\text{N}_4/\text{h-BN}$ hybrids and binary $\text{g-C}_3\text{N}_4/\text{Au}$ NPs exhibit a positive shift of ~ 0.1 eV as compared to that of pure $\text{g-C}_3\text{N}_4$. Then, a further positive shift of ~ 0.1 eV can be also found on the $\text{g-C}_3\text{N}_4/\text{h-BN}/\text{Au}$ NPs (Fig. 3(a)), implying the stronger interface interaction formed in the ternary nanocomposites. On the contrary, the obvious negative shifts of N 1 s and B 1 s are then detected on the resultant $\text{g-C}_3\text{N}_4/\text{h-BN}/\text{Au}$ NPs in comparison with the reference samples (Fig. 3(b–c)). In detail, the XPS pattern of N 1 s originated from the initial $\text{g-C}_3\text{N}_4$ sample would be fitted with two peaks (Fig. 3(b)), and the strong peak at 398.8 eV is assigned to $\text{C}=\text{N}-\text{C}$ groups while the weak peak at 400.2 eV is related to $\text{N}-(\text{C})_3$ groups [5,8]. Compared with the bare $\text{g-C}_3\text{N}_4$, the main peak of N 1 s is located at 398.7 eV and 398.6 eV for the binary $\text{g-C}_3\text{N}_4/\text{Au}$ NPs and ternary nanocomposites, respectively. Analogously, the dominant peak of B 1 s at 189.3 eV derived from hybrid $\text{g-C}_3\text{N}_4/\text{h-BN}$ slightly shifts to 189.2 eV for binary $\text{h-BN}/\text{Au}$ NPs and ternary $\text{g-C}_3\text{N}_4/\text{h-BN}/\text{Au}$ NPs, as displayed in Fig. 3(c). On the other hand, the double features of Au 4 f at about 82.2 eV and 85.8 eV originated from binary $\text{g-C}_3\text{N}_4/\text{Au}$ NPs or $\text{h-BN}/\text{Au}$ NPs are also negative shift to 82.1 eV and 85.7 eV for the ternary $\text{g-C}_3\text{N}_4/\text{h-BN}/\text{Au}$ NPs (Fig. 3(d)). Compared with reference samples, both positive shifts of C 1 s and negative shifts of N 1 s, B 1 s and Au 4 f can be found on the resultant $\text{g-C}_3\text{N}_4/\text{h-BN}/\text{Au}$ NPs. It implies the modified electronic structures of heterointerfaces via high electron transfer among these components [19–21,46–49], supporting the coexistence of a strong synergistic coupling effect at their connected interfaces.

Then, the optical-electrical properties of the generated $\text{g-C}_3\text{N}_4/\text{h-BN}/\text{Au}$ NPs and the mentioned four references were further evaluated to get a deep insight into the strong synergistic coupling effect among ternary nanocomposites. The photoluminescence (PL) spectra presented

in Fig. 4(a) are used to illustrate the photoexcited carrier separation efficiency in the obtained $\text{g-C}_3\text{N}_4/\text{h-BN}/\text{Au}$ NPs. In fact, the lower PL intensity usually implies the higher separation of photogenerated electron-hole pairs on semiconductors, since the PL spectra are mainly derived from energy emission during the recombination of photoinduced carriers [8]. As shown in Fig. 4(a), it is found that the lowest PL intensity is definitely detected on the resultant $\text{g-C}_3\text{N}_4/\text{h-BN}/\text{Au}$ NPs in comparison with other reference samples. In detail, the PL intensity of ternary $\text{g-C}_3\text{N}_4/\text{h-BN}/\text{Au}$ NPs at ~ 430 nm is measured at ~ 2530 a.u which is only about three out of twenty than that of the initial $\text{g-C}_3\text{N}_4$ nanoplates. It reveals the suppressed recombination and then enhanced separation efficiency of photoexcited electron-hole pairs on the resultant $\text{g-C}_3\text{N}_4/\text{h-BN}/\text{Au}$ NPs, which can be also verified by the time-resolved emission decay spectra (Fig. 4(b)). According to the experimental data in Fig. 4(b), the average luminescence lifetimes for different samples were then estimated in the inset table, and the shortest value would be also found on the ternary $\text{g-C}_3\text{N}_4/\text{h-BN}/\text{Au}$ NPs in comparison with the other references. Subsequently, the transient photocurrent responses of different samples are carried out to illustrate the photoexcited carriers transfer (Fig. 4(c)), which were recorded through the incident light were switched on and off in intervals of 20 s. Notably, the photocurrent density of the resultant $\text{g-C}_3\text{N}_4/\text{h-BN}/\text{Au}$ NPs is significantly higher than that of the other reference samples, supporting the much higher efficient migration of photoexcited charge carriers on the ternary nanoproducts. The corresponding photocurrent density is measured as high as ~ 0.47 μA , which is already 5.1, 8.2, 8.3 and 10.3 times higher than that of the hybrid $\text{g-C}_3\text{N}_4/\text{h-BN}$, $\text{g-C}_3\text{N}_4/\text{Au}$ NPs, $\text{h-BN}/\text{Au}$ NPs and original $\text{g-C}_3\text{N}_4$, respectively. The remarkable enhancement manifests that the ternary $\text{g-C}_3\text{N}_4/\text{h-BN}/\text{Au}$ NPs have a greater ability to accelerate the migration/transmission of photogenerated charge carriers. Moreover, the

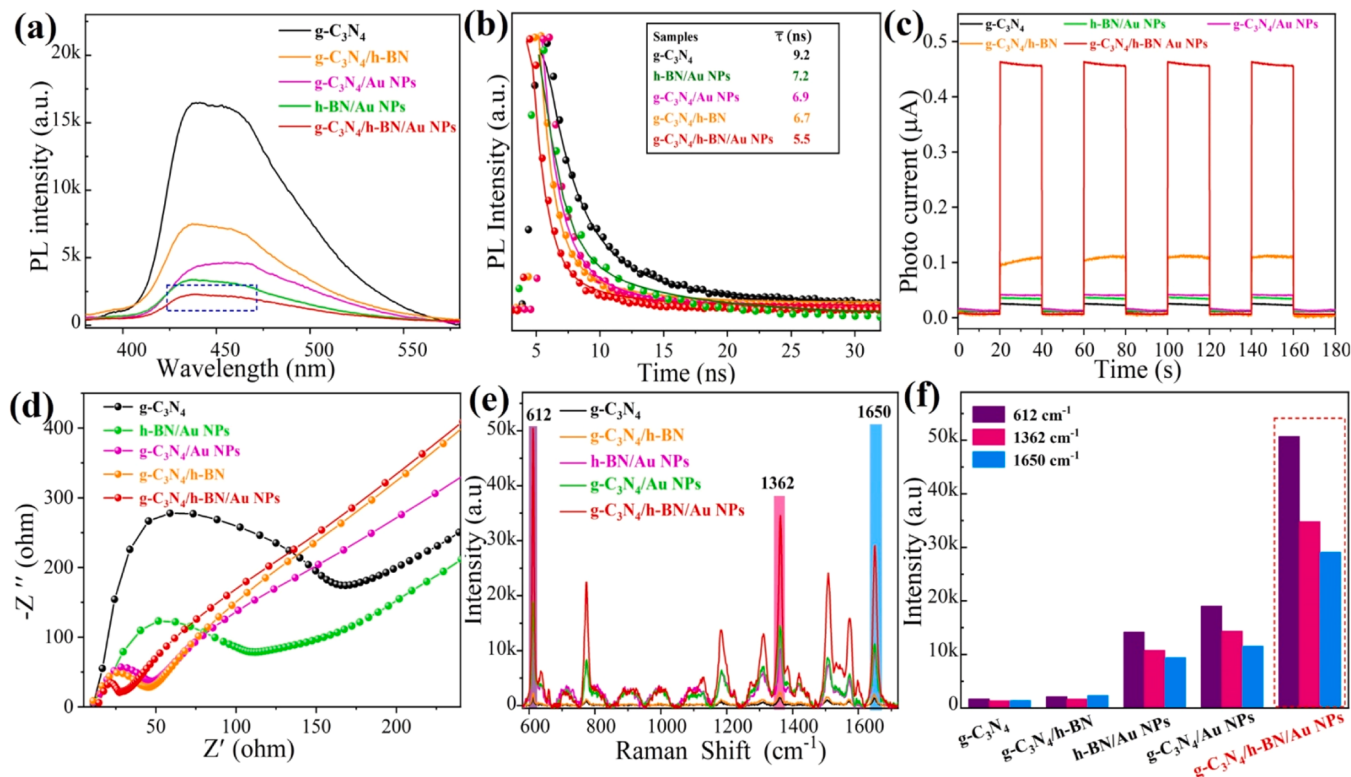


Fig. 4. Optical-electrical properties of the prepared $\text{g-C}_3\text{N}_4/\text{h-BN/Au NPs}$ and reference samples (original $\text{g-C}_3\text{N}_4$, hybrid $\text{g-C}_3\text{N}_4/\text{h-BN}$, binary $\text{g-C}_3\text{N}_4/\text{Au NPs}$ and h-BN/Au NPs). (a-b) The PL spectra and time-resolved emission decay spectra, (c) the transient photocurrent responses excited by the xenon lamp light irradiation, (d) EIS Nyquist plots, (e-f) Raman spectra of 10^{-6} M R6G probe molecules adsorbed on the above nano-substrates and the variations of Raman peak intensities at 612, 1362 and 1650 cm^{-1} versus for different nano-substrates.

electrochemical impedance spectra (EIS) measurements (Fig. 4(d)) demonstrate the interfacial charge transfer behaviors of different samples. As expected, the obtained $\text{g-C}_3\text{N}_4/\text{h-BN/Au NPs}$ exhibit a smaller impedance arc radius than that of the other references, confirming an obvious reduction of charge transfer resistance and then giving rise to the more efficient carrier transfer at the interface regions. Then, the surface-enhanced Raman scattering spectroscopy (SERS) tests of R6G probe molecules adsorbed on the above different nano-substrates, further reveal the photo-induced carrier transfer (PICT) efficiency of each sample (Fig. 4(e-f)). The boosted SERS activity is highly related to the remarkable PICT efficiency since it is beneficial for both improving LSPR-induced electromagnetic (EM) enhancement and promoting charge transfer (CT)-triggered chemical enhancement (CE) [53–56]. As displayed in Fig. 4(e), the characteristic bands of R6G molecules are clearly detected in Raman spectra, including strong ring C-C stretching vibration at 612 cm^{-1} , ring skeletal vibration of radical orientations at 1362 cm^{-1} and ring C-H bends at 1650 cm^{-1} , etc. [53]. It can be seen that considerably stronger Raman signals of probe molecules are recorded on the resultant $\text{g-C}_3\text{N}_4/\text{h-BN/Au NPs}$ as compared to the other references. Meanwhile, the enhanced SERS performance would be also obviously confirmed by the variations of Raman peak intensities at versus different nano-substrates in Fig. 4(f). For instance, the Raman peak of R6G molecules at 612 cm^{-1} is dramatically increased from about 1696 a.u to ~ 50703 a.u when the nano-substrates changed from the pristine $\text{g-C}_3\text{N}_4$ to the obtained $\text{g-C}_3\text{N}_4/\text{h-BN/Au NPs}$, offering ~ 30 -fold enhancement in SERS performance. So, the remarkably enhanced PICT efficiency can be verified on the obtained ternary nanocomposites, supporting the improved separation and accelerated transmission of photogenerated charge carriers [57,58]. The established $\text{g-C}_3\text{N}_4/\text{h-BN/Au NPs}$ with strong synergistic coupling effect within ternary components are expected to provide more admirable PTC degradation performance, which will be illustrated in the following

sections.

3.2. Photo-thermal catalytic degradation

3.2.1. Fantastic PTC activity

Based on the resultant $\text{g-C}_3\text{N}_4/\text{h-BN/Au NPs}$, the predominant goal of this work is to verify the excellent PTC activity toward high-performance degradation of aqueous pollutants. Firstly, the broadband light ($>400 \text{ nm}$)-derived PTC degradation performance of R6G dyes in alkaline solution ($\text{pH}\sim 11.2$) is illustrated in Fig. 5(a), which can be simply revealed by the time-dependence evolution of absorption peak intensity of dyes during the catalytic reaction. Before each degradation test, the as-prepared reactive solution was carefully kept in a dark condition for 30 min. The absorption peak intensity of R6G dyes at about 520 nm would slightly reduce and tend to be stable at the late stage (Fig. 5(a)), reflecting the adsorption-desorption equilibrium between catalysts and molecules. In the presence of $\text{g-C}_3\text{N}_4/\text{h-BN/Au NPs}$, the absorption peak intensity of R6G dyes gradually decreases with the increasing light illumination time (0–20 min), supporting the residual molecular concentration continuously reduces during the PTC degradation. After 20 min irradiation, there are nearly no R6G dyes left in the solution since the corresponding absorption peak is too weak to be detected in Fig. 5(a). It implies the complete elimination of dyes from wastewater by high-performance PTC reaction, which can be also illustrated by the color change of the reactive solution from initial orange to colorless after 20 min irradiation (inset in Fig. 5(a)). By comparison, the absorption peak evolutions of R6G dyes in the presence of the reference nano-catalysts demonstrate that some residual R6G dyes were retained in solution after the same 20 min irradiation, implying the relatively low PTC degradation performances (Fig. S8). By comparing the absorption peak intensity with that of the pristine one, the PTC degradation efficiencies of different nano-catalysts are evaluated by the

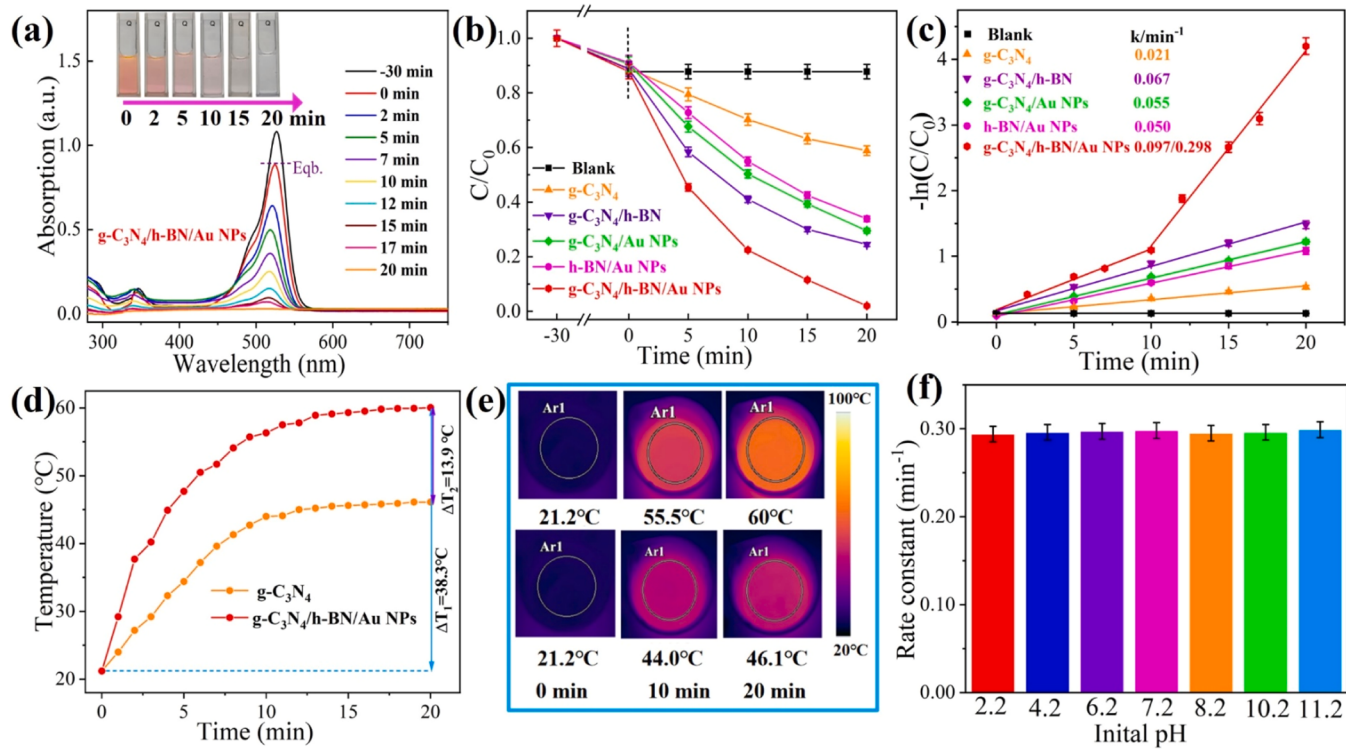


Fig. 5. (a) Broadband light (>400 nm)-driven PTC degradation of R6G dyes in alkalic ($\text{pH} \sim 11.2$) solution based on the obtained $\text{g-C}_3\text{N}_4/\text{h-BN}/\text{Au NPs}$, the inset in (a) shows the color change of the organic solution from initial orange to colorless at the late reaction. (b) PTC degradation efficiencies of different nano-catalysts including the resultant $\text{g-C}_3\text{N}_4/\text{h-BN}/\text{Au NPs}$, and reference samples (original $\text{g-C}_3\text{N}_4$, hybrid $\text{g-C}_3\text{N}_4/\text{h-BN}$, binary $\text{g-C}_3\text{N}_4/\text{Au NPs}$ and $\text{h-BN}/\text{Au NPs}$), (c) the calculated results of fitting data to pseudo-first-order kinetics and corresponding k values, respectively. (d) Temperature evolutions of two different solutions in the presence of ternary $\text{g-C}_3\text{N}_4/\text{h-BN}/\text{Au NPs}$ and pristine $\text{g-C}_3\text{N}_4$ powers irradiated by one-sun light (1 kW/m^2), (e) the corresponding IR thermal images of the above two samples at different irradiation time. (f) The variation of PTC degradation efficiencies of $\text{g-C}_3\text{N}_4/\text{h-BN}/\text{Au NPs}$ toward the degradation of R6G dyes in acidic-neutral-alkallic solutions ($\text{pH}: 2.2\text{--}11.2$), and the light source with xenon lamp (1 kW/m^2) irradiation of 20 min was selected in the above each test.

variations of (C/C_0) within the same 20 min irradiation (Fig. 5(b)). Obviously, there is nearly 99.93% degradation efficiency can be achieved by using the obtained $\text{g-C}_3\text{N}_4/\text{h-BN}/\text{Au NPs}$, implying the highly efficient degradation of dyes. Meanwhile, the TOC and COD removal rates (Fig. S9) can be separately calculated at about 76.8% and 61.1% after 20 min irradiation, which is lower than the above-measured degradation efficiency due to the formation intermediate by products during the mineralization or chemical oxidation. As shown in Fig. 5(b), on the other hand, there are about 78%, 69%, 64% and 38% degradation efficiencies obtained from the reference $\text{g-C}_3\text{N}_4/\text{h-BN}$, $\text{g-C}_3\text{N}_4/\text{Au NPs}$, $\text{h-BN}/\text{Au NPs}$, and pristine $\text{g-C}_3\text{N}_4$, respectively. As for each nanocatalysts, the relationship between the $\ln(C/C_0)$ and light irradiation time is then separately displayed in Fig. 5(c), based on the PTC degradation obeys the pseudo-first-order kinetics ($C = C_0 e^{-kt}$, k is the degradation rate constant) [6,8,19,20,28]. There are two different linearized plot regions for responding to the two PTC degradation activities of the resultant $\text{g-C}_3\text{N}_4/\text{h-BN}/\text{Au NPs}$ (red line in Fig. 5(c)), which is also consistent with our recent work [8]. The two linearized plot regions can be roughly divided into a slow reaction kinetics at the initial stage of 0–10 min and a rapid dynamic region at the late stage of 10–20 min. It is obviously different from the traditional photocatalysts with a single linearity for each reference sample in Fig. 5(c). Furthermore, the optimal degradation rate constant of $\text{g-C}_3\text{N}_4/\text{h-BN}/\text{Au NPs}$ is calculated as high as about 0.298 min^{-1} at the late stage of 10–20 min, which is much higher than that (0.097 min^{-1}) at the initial state and also superior to the reference samples and most of the previous works (Comparison analysis in Table S1 in SI). On the other hand, the PTC degradations of ciprofloxacin (CIP) antibiotics and pendimethalin (PDM) pesticides in the presence of $\text{g-C}_3\text{N}_4/\text{h-BN}/\text{Au NPs}$ can also confirm the higher degradation activity at the late stage of light irradiation (Fig. S10). The

enhanced PTC degradation efficiency at the rapid dynamic region is mainly attributed to the highly-efficient photo-thermal conversion of the ternary $\text{g-C}_3\text{N}_4/\text{h-BN}/\text{Au NPs}$. It enables more thermal energy derived from broadband light irradiation to be effectively utilized for promoting PTC activity, which has been carefully illustrated in our recent work [8]. To verify it, the elevated temperatures of two different solutions in the presence of the $\text{g-C}_3\text{N}_4/\text{h-BN}/\text{Au NPs}$ and reference $\text{g-C}_3\text{N}_4$ are separately illustrated by one-sun light (1 kW/m^2) irradiation of 20 min, as shown in Figs. 5(d)–5(e). As for the resultant $\text{g-C}_3\text{N}_4/\text{h-BN}/\text{Au NPs}$, the temperature of the solution rapidly increases from an initial $21.2\text{--}60^\circ\text{C}$ after 20 min light irradiation, whereas the elevated temperature is only reached at $\sim 46.1^\circ\text{C}$ via bare $\text{g-C}_3\text{N}_4$. Meanwhile, the nitrogen (N_2) adsorption-desorption isotherms of the above two samples (Fig. S11) reveal that the specific surface area of $\text{g-C}_3\text{N}_4/\text{h-BN}/\text{Au NPs}$ is calculated $\sim 29.2 \text{ m}^2/\text{g}$ via Brunaure-Emmett-Teller (BET) method [4], which is higher than that of the reference bare $\text{g-C}_3\text{N}_4$ ($\sim 16.9 \text{ m}^2/\text{g}$). Moreover, the temperature-dependent degradations of R6G dyes in the presence of $\text{g-C}_3\text{N}_4/\text{h-BN}/\text{Au NPs}$ at different constant heating solutions controlled by water-cooling equipment are illustrated in this work (Fig. S12(a)). It reveals the thermal-assisted degradation performance at higher temperature condition, owing to the higher transmission efficiency of photoexcited charge carriers verified by temperature-dependent PL spectra (Fig. S12(b)). Therefore, the resultant $\text{g-C}_3\text{N}_4/\text{h-BN}/\text{Au NPs}$ with large surface area can possess improved photo-thermal conversion and higher utilization of thermal energy in comparison with the reference samples, offering significant thermal-assisted contribution for boosting PTC degradation efficiency. As for the R6G dyes used in this work, the possible intermediates and final product formations during the PTC degradation process were also illustrated through LC/MS measurement (Fig. S13). Subsequently, the variations of PTC degradation efficiency

performed in acidic-neutral-alkaline solutions (pH: 2.2–11.2) were carried out to explore the application potential of the resultant g-C₃N₄/h-BN/Au NPs in the different real environments (Fig. 5(f)). The g-C₃N₄/h-BN/Au NPs show reliable and stable PTC degradation performance in a wide pH range, supporting the universal applicability of the obtained PTC nano-catalysts.

To reveal the reactive species in the PTC degradation, the trapping experiments in the presence of the resultant g-C₃N₄/h-BN/Au NPs were carried out by selecting L-AA, AO and IPA molecules as capture scavengers of oxide-free ($\bullet\text{O}_2^-$), holes (h^+) and hydroxyl ($\bullet\text{OH}$), respectively (Fig. 6(a)). It can be seen that the degradation rate of the new PTC nano-catalysts can be obviously inhibited by the addition of L-AA and AO scavengers. In detail, the degradation rate is separately reduced from $\sim 0.298 \text{ min}^{-1}$ at the pristine one to about 0.106 min^{-1} or 0.184 min^{-1} in the presence of L-AA or AO scavengers. By comparison, the degradation efficiency is not easily influenced by adding IPA scavengers, since the degradation rate is slightly changed to about 0.214 min^{-1} (Fig. 6(a)). Moreover, the contribute proportions of the above three species in PTC degradation (inset in Fig. 6(a)) further reveal that the contribute percentages of $\bullet\text{O}_2^-$ radicals and h^+ species are evaluated about 49.2% and 29.2%, and residual $\sim 21.6\%$ is attributed to $\bullet\text{OH}$ radicals. Therefore, the $\bullet\text{O}_2^-$ radicals and h^+ species should be regarded as the two main reactive species for the PTC degradation in the presence of as-prepared g-C₃N₄/h-BN/Au NPs. Furthermore, the electron paramagnetic resonance (EPR) spectra with 5,5-dimethyl-pyrroline-N-oxide (DMPO) and 2,2,6,6-tetramethyl-1-piperidinyloxy (TEMPO) were separately explored to reveal the $\bullet\text{O}_2^-$ radicals and $\bullet\text{OH}$ species formed on the

obtained PTC nano-catalysts (Fig. 6(b–c)). Clearly, the ESR signals of DMPO-assisted $\bullet\text{O}_2^-$ radicals are more obvious in both methanol and aqueous mediums under light irradiation than under dark conditions, verifying the dominant roles of $\bullet\text{O}_2^-$ radicals. Meanwhile, the strong EPR peak intensities of TEMPO-assisted h^+ species (black curve Fig. 6(d)) distinctly become weak upon extending the solar light irradiation time to 5 min. As for the generated g-C₃N₄/h-BN/Au NPs, the apparently consumed h^+ species convincingly suggest that they can directly participate in the PTC degradation. On the other hand, similar trapping experiments based on the reference nano-catalysts of binary g-C₃N₄/Au NPs were also performed in this work (Fig. S14). Different from the resultant g-C₃N₄/h-BN/Au NPs, there is only $\bullet\text{O}_2^-$ radicals can play an important role in the presence of the reference sample and the h^+ species have little effect in the degradation process. In detail, the contribute percentage of $\bullet\text{O}_2^-$ radicals is achieved at $\sim 77.6\%$, whereas only about 8.1% and 14.3% as for h^+ species and $\bullet\text{OH}$ radicals (Fig. S14 (a)). Meanwhile, the obvious ESR signals of DMPO-assisted $\bullet\text{O}_2^-$ radicals would be merely detected in methanol medium under light irradiation and then disappeared in aqueous solution (Fig. S14(b–c)). Moreover, the EPR signals of TEMPO-assisted h^+ species after 5 min light irradiation are very close to the pristine ones at initial dark condition (Fig. S14 (d)), implying that the h^+ species formed in the reference sample cannot effectively participate in the PTC degradation. It is well-known that the $\bullet\text{O}_2^-$ radicals are mainly derived from the photoexcited electrons on the surfaces of semiconductor-based photocatalysts ($\text{O}_2 + \text{e}^- \rightarrow \bullet\text{O}_2^-$) and the formation of $\bullet\text{OH}$ radicals should be highly related to the h^+ species ($\text{h}^+ + \text{OH} \rightarrow \bullet\text{OH}$) [4–10, 14–15]. Compared to the reference g-C₃N₄/Au

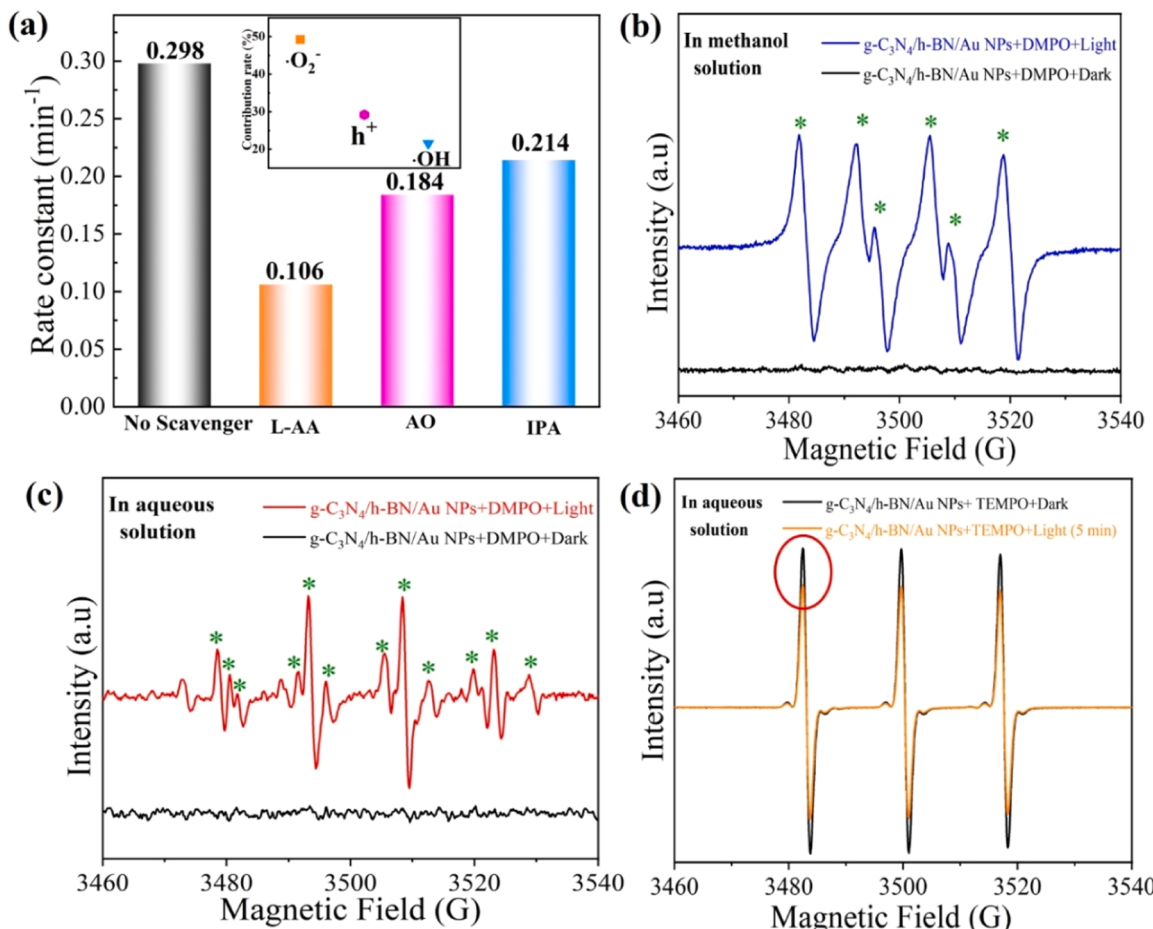


Fig. 6. (a) Based on the obtained g-C₃N₄/h-BN/Au NPs, the trapping experiments of reactive species during PTC degradation via different scavengers (IPA→ $\bullet\text{OH}$, L-AA→ $\bullet\text{O}_2^-$ and AO→ h^+), the inset shows the contribute proportions of different reactive species in PTC degradation, (b-d) EPR spectra of DMPO- $\bullet\text{O}_2^-$ in methanol and aqueous solution, TEMPO- h^+ , respectively.

NPs-based photocatalysts, the resultant g-C₃N₄/h-BN/Au NPs explicitly enable both photoexcited electrons and holes to be efficiently utilized in PTC degradation, offering a double-effect for promoting degradation efficiency.

3.2.2. Unprecedented PTC Stability

Besides the ultrahigh PTC activity, more importantly, the distinctive superiority of the obtained g-C₃N₄/h-BN/Au NPs should be also highlighted in terms of exceptional PTC recyclability toward reusable long-term practical operation. To verify it, the repeated PTC degradation tests of R6G dyes in alkalic solution based on the resultant g-C₃N₄/h-BN/Au NPs and reference g-C₃N₄/Au NPs were carefully carried out in this work. The detailed comparisons of the corresponding PTC degradation efficiencies during 10 consecutive recycling tests within 500 min are illustrated in Fig. 7(a). As for the generated g-C₃N₄/h-BN/Au NPs, the excellent PTC recyclability can be convincingly manifested on the obtained nano-catalysts, since the remaining 99.8% degradation efficiency can be well maintained after repeated 10 tests within 500 min. By comparison, there is only about 42.4% PTC degradation efficiency would be reserved after the same repeated tests in the presence of the reference g-C₃N₄/Au NPs. The great challenge of PTC recyclability is strongly related to the broadband light-heated high temperature that can dramatically accelerate the photocorrosion-induced deactivation of nano-catalysts, which is obviously different from the conventional recycling tests under room temperature in most previous works. Based on the resultant g-C₃N₄/h-BN/Au NPs, the time-dependence evolutions of PTC degradation performances of R6G dyes in the steady heated

(60 °C) aqueous condition during 10 h consecutive measurements were then performed in this work (Fig. S15(a)). It can be found that the PTC degradation efficiency after continuous operation at 60 °C high temperature condition is nearly identical to that of the pristine one at the initial stage, confirming the satisfactory PTC thermostability of the resultant g-C₃N₄/h-BN/Au NPs. Moreover, the long-term PTC stabilities of the established nano-catalysts and reference g-C₃N₄/Au NPs were further evaluated by interval degradation tests within 15 days (Fig. S15(b)). As expected, the obtained g-C₃N₄/h-BN/Au NPs exhibit considerable long-term PTC stability with a remaining degradation efficiency of ~99% after keeping them for 15 days. In regard to the residual PTC activity after recycling tests, the detailed comparisons of the obtained g-C₃N₄/h-BN/Au NPs and other previous nano-catalysts are carefully illustrated in this work (Fig. 7(b)), and the detailed comparisons in Table S2 in SI. Considering the repeated cycles and remaining degradation efficiencies, the sharp contrasts explicitly confirm the remarkably improved PTC reusability of g-C₃N₄/h-BN/Au NPs in comparison with many other nano-catalysts in previous works. Therefore, these obvious comparisons intuitively reveal the remarkable advantage of the resultant g-C₃N₄/h-BN/Au NPs with unprecedented PTC recyclability in the repeated degradation of organic pollutants at high temperature condition, which is more suitable for propelling long-term practical wastewater purifications.

In order to further evaluate the microstructural stability of the prepared g-C₃N₄/h-BN/Au NPs, we performed the TEM, XRD and Raman spectra tests of the same nano-catalysts before and after keeping them in different corrosive and harsh environments. Fig. 8(a)-(b) show the TEM

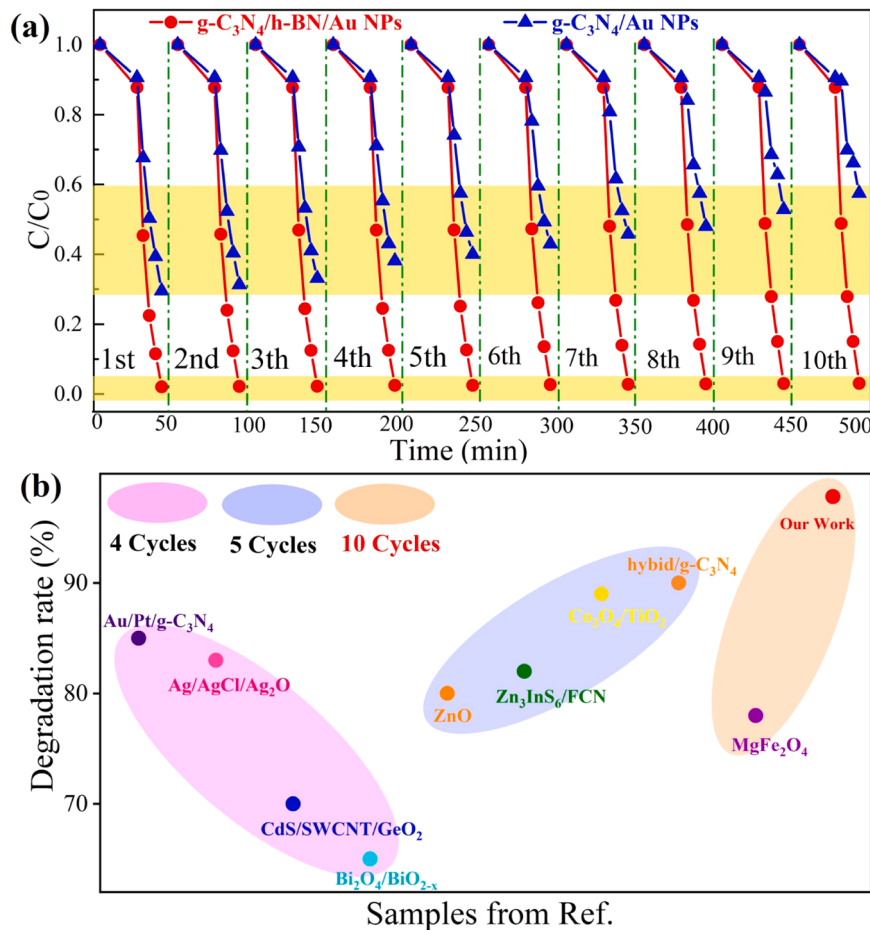


Fig. 7. (a) The repeated PTC degradation tests of R6G dyes in alkalic (pH~11.2) solution based on the obtained g-C₃N₄/h-BN/Au NPs and reference g-C₃N₄/Au NPs, (b) the comparison analysis of residual PTC activity after recycling tests in the presence of the resultant g-C₃N₄/h-BN/Au NPs and other nano-catalysts developed in previous literatures.

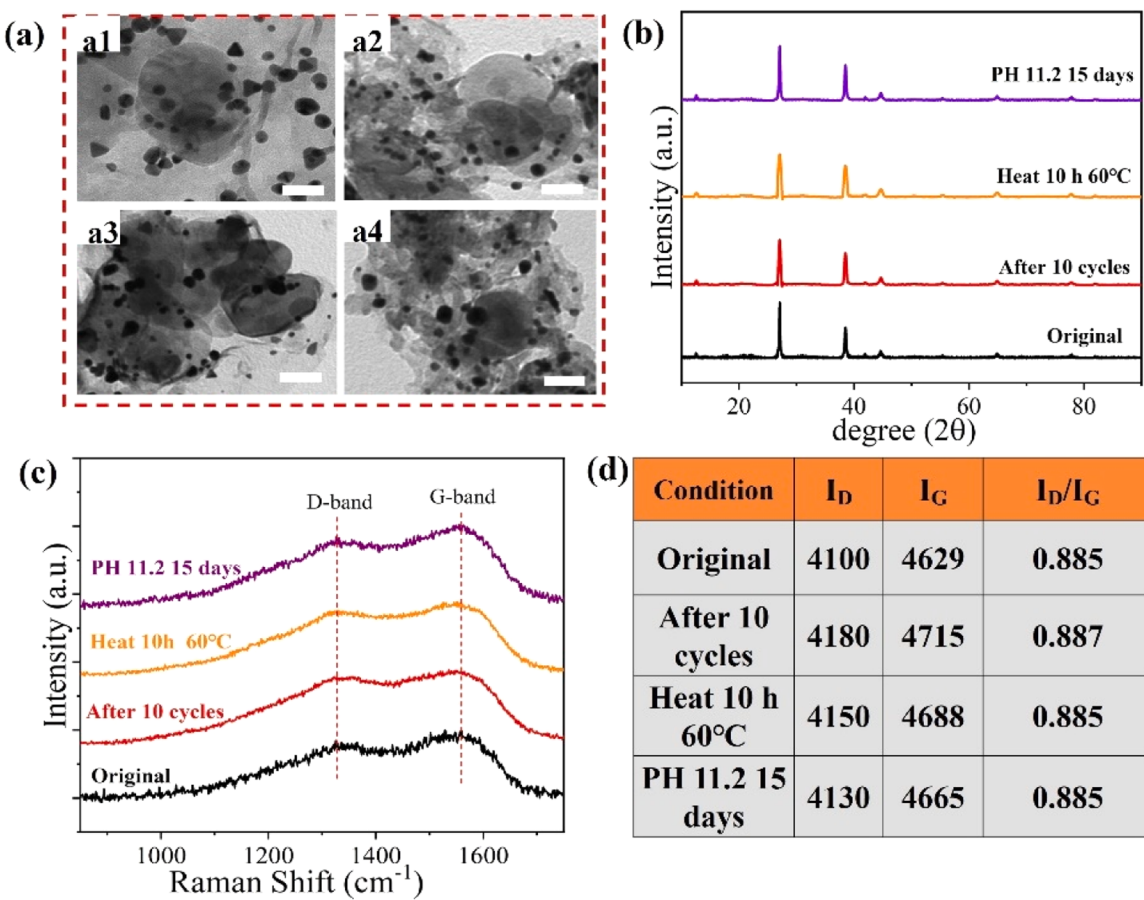


Fig. 8. The microstructural stability of the generated g-C₃N₄/h-BN/Au NPs after keeping them in different corrosive and harsh environments. (a-b) the TEM images and XRD patterns of the original one and the used target after 10 recycling PTC degradation tests and two samples after remaining in alkalic (pH: ~11.2) corrosive solutions for 15 days and in heated (60 °C) liquid for 10 h, respectively, (c-d) the Raman spectra and the corresponding calculated results of the G-band and D band originated from 2D supports at different conditions.

images and XRD patterns of the pristine one, the used target after 10 recycling PTC degradation tests, and the two samples after keeping them in alkalic (pH: ~11.2) corrosive solutions for 15 days and in heated (60 °C) liquid condition for 10 h, respectively. After undergoing the above different treatments, it can be found that the treated g-C₃N₄/h-BN/Au NPs maintain identical micro-topographies in comparison with the initial one. For example, the abundant plasmonic Au NPs can be also loaded on 2D g-C₃N₄/h-BN supports and there is no obvious dissolution of these composites after repeated 10 degradation tests (Fig. 8(a1)). Meanwhile, the EDS patterns of these treated samples (Fig. S16) are also consistent with the pristine one (Fig. S3(c)), confirming the reliable chemical stability of the ternary g-C₃N₄/h-BN/Au NPs even after alkalic corruptions for 15 days or thermal treatment for 10 h. Moreover, the XRD patterns of the pristine g-C₃N₄/h-BN/Au NPs and these treated samples further reveal excellent stable crystal phases of the nanocomposites owing to the very similar XRD peaks detected on each target (Fig. 8(b)). On the other hand, the Raman spectra of the above-mentioned nanocomposites are recorded and then used to demonstrate stable 2D structures of g-C₃N₄/h-BN supports in the resultant g-C₃N₄/h-BN/Au NPs. As displayed in Fig. 8(c), there are two broad peaks detected at about 1350 cm⁻¹ and 1570 cm⁻¹ in the Raman spectra of each sample, which can be attributed to the vibrational D-band and G-band characteristic peaks of carbon-related materials, respectively. The two Raman signals of the D-band and G-band are generally originated from the disordered sp² microdomains via breathing mode of k-point photons of A_{1g} symmetry and symmetric E_{2g} vibrational mode in graphite-like sp² carbon lattice, respectively [59–61]. As expected, the two Raman peaks of the D-band and G-band originating from the pristine g-C₃N₄/h-BN/Au

NPs can be well repeated on the three treated samples (Fig. 8(c)). Furthermore, the corresponding I_D/I_G (the ratio of D-band peak intensity and G-band peak intensity) values were calculated and illustrated in this work (Fig. 8(d)), reflecting the detailed change of 2D supports with disordered structures or defects. Indeed, the nearly identical value of I_D/I_G in the narrow range of 0.885–0.887 derived from each target can further manifest the excellent stable 2D structures in the resultant g-C₃N₄/h-BN/Au NPs. Briefly, the newly generated PTC nano-catalysts with stable microstructures can be robust enough to withstand recyclable degradation in harsh environments and high temperature conditions.

3.2.3. Mechanisms of superactive and ultrastable PTC system

The mechanisms of the resultant g-C₃N₄/h-BN/Au NPs with superactive degradation efficiency and unparalleled thermostability were rationally illustrated in this work (Fig. 9, Fig. S17–22). As for the established ternary g-C₃N₄/h-BN/Au NPs, the three components play different roles in improving PTC degradation performances. Firstly, the main PTC active constituent is attributed to the polymeric layered g-C₃N₄ semiconductors with narrow-band structures (Fig. 2(d)), which can enhance the broadband light absorption capacity at the visible-NIR region (>400 nm). The loaded plasmonic Au NPs with unique LSPR also provide plentiful photoexcited energetic hot carriers for further accelerating PTC reaction rate under resonant visible light (500–600 nm) irradiation. The two components in the ternary g-C₃N₄/h-BN/Au NPs give rise to stronger photon-excitation efficiency and higher photo-thermal conversion in comparison with the traditional binary g-C₃N₄/Au NPs-based reference samples. So, it is not only beneficial to the

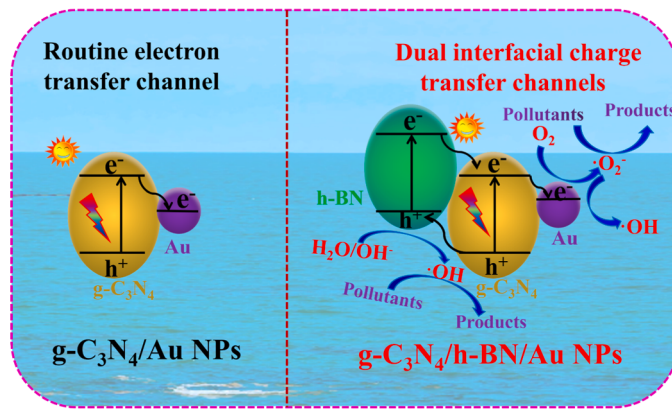


Fig. 9. Schematic illustration of the PTC enhancement mechanisms in the resultant $\text{g-C}_3\text{N}_4/\text{h-BN}/\text{Au}$ NPs toward high-efficiency degradation under broadband light irradiation.

generation of abundant energetic carriers via direct photon-excitation but also conducive to the reutilization of broadband light-driven thermal energy for providing another contribution to the catalytic reaction. The mentioned PTC mechanisms have been convincingly confirmed and detailedly demonstrated in our recent work [8], which is also coincident with this case. Besides, the enhanced PTC activity should be also attributed to the ingenious construction of dual-interfacial charge carrier transfer channels in the obtained $\text{g-C}_3\text{N}_4/\text{h-BN}/\text{Au}$ NPs. Superior to traditional nano-catalysts with a single carrier channel in each sample, the hybrid $\text{g-C}_3\text{N}_4/\text{h-BN}/\text{Au}$ NPs give rise to the simultaneous and separate extraction of photoexcited holes and electrons on the extraordinary heterostructures. On the one hand, the conventional electron transfer channel can be formed at the connected interfaces between $\text{g-C}_3\text{N}_4/\text{h-BN}$ semiconductor components and plasmonic Au NPs, since the work function of the dominant Au (111) or (200) crystal plane is higher than that of 2D semiconductor supports [20,33,35,37,46,59,62]. It can lead to the formation of the Schottky barrier on their interfaces, significantly facilitating the transfer of photoexcited electrons from the semiconductor components to the plasmonic metallic Au NPs [62–64]. The above deductions were carefully verified by a series of experimental measurements and theoretical simulations according to the USP, XPS, VB spectra, Mott-Schottky plots (Fig. S17) and DFT calculations (Fig. S18–20), and the detailed descriptions (conduction-band structures, valence-band structures, work functions, charge densities and electron transfer paths, etc.) are shown in *Supporting information*. On the other hand, the thermally and chemically stable 2D h-BN nanosheets with inherent large band-gap of ~ 5.3 eV have been also characterized by excellent electronegativity [65–67], which can be regarded as perfect electrical insulators due to the reduced electron-delocalization in BN π bounds [38–40]. If the electrically insulating nanoplates are decorated with other semiconductors, the negatively charged h-BN components have the ability to attract the photoexcited holes from band-gap semiconductors under broadband light irradiation [63–67]. In this regard, the h-BN nanoplates were carefully examined by zeta-potential test, and the measured negative surface charge of about -23.1 mV (Fig. S21) convincingly verifies the intrinsic electronegativity of 2D h-BN components in this work. As for the PTC degradation in the presence of $\text{g-C}_3\text{N}_4/\text{h-BN}/\text{Au}$ NPs under broadband light excitation, the 2D h-BN insulators can be served as effective hole-acceptors for accelerating the photoexcited holes transfer from the narrow band-gap $\text{g-C}_3\text{N}_4$ semiconductors to the negatively charged components. Therefore, the unique dual charge carrier transfer channels formed in the resultant $\text{g-C}_3\text{N}_4/\text{h-BN}/\text{Au}$ NPs are extremely conductive to effectively separate photogenerated electrons and holes, offering more plentiful energetic carriers for improving PTC degradation reaction. Meanwhile, the high-efficiency degradation is still related to the strong connection

between the organic dyes and nano-catalysts, which can be verified by the higher absorption capacity of R6G dyes based on the theoretical comparison of absorption energy of R6G molecules on the obtained $\text{g-C}_3\text{N}_4/\text{h-BN}/\text{Au}$ NPs and the reference $\text{g-C}_3\text{N}_4/\text{Au}$ NPs (Fig. S22). Besides the above ultrahigh PTC activity, the unprecedented thermostability of $\text{g-C}_3\text{N}_4/\text{h-BN}/\text{Au}$ NPs is also ascribed to the established dual interfacial charge transfer channels on the ternary heterostructures. As is well known, the poor stability of semiconductor nano-catalysts is mainly attributed to their serious self-oxidation of themselves via the severe accumulation of excess photogenerated holes on their surfaces [14–17]. In this work, the remarkably inhibited photocorrosion should be originated from the efficient transformation of photoexcited holes from oxidation-sensitive $\text{g-C}_3\text{N}_4$ to thermally stable h-BN insulators with excellent antioxidant capacity, giving rise to the exceptional photostability toward long-term repeated PTC degradation at high temperature condition. Previously, the accumulation of charge carriers on semiconductors has been effectively suppressed by introducing dual-cocatalysts that can separately attract photogenerated holes and electrons toward HER/OER or CO_2 reduction [30–34]. Superior to these reported metallic oxides/sulfides-based cocatalysts, the h-BN insulators adopted in this work are indeed more thermally/chemically stable 2D structures. Importantly, the negatively charged h-BN nanosheets can also avoid the strict alignment of electronic states in hetero-interfaces that limit the effective transmission of photoexcited electropositive holes. Therefore, the adopted unique 2D h-BN supports are then regarded as excellent stable-structured acceptors for extracting the photoexcited holes from $\text{g-C}_3\text{N}_4$ in this work. Then, the remarkably reduced accumulation of photogenerated holes on the unstable $\text{g-C}_3\text{N}_4$ components will also significantly suppress the possible self-oxidative decomposition process of nitrogen anions to N_2 ($2 \text{N}^{3-} + 6 \text{h}^+ \rightarrow \text{N}_2$) [14, 37, 41–43]. Therefore, the probable mechanisms of the ultrahigh activity and extraordinary long-term recyclability at high temperature conditions are illustrated in the above reasonable manners, giving insight into the distinctive advantages of the newly generated PTC nano-catalysts.

3.3. Practical PTC degradation of organic pollutants in real-world scenarios

Based on the superactive and ultrastable $\text{g-C}_3\text{N}_4/\text{h-BN}/\text{Au}$ NPs, the newly generated PTC nano-catalysts were extended to the repeated degradations of organic R6G pollutants at large-volume level (10 mg/L, 5 L) solution and then practically applied to the recycling decontaminations of actual water samples in real-world scenarios. Traditionally, the existing drawback in wastewater purification is that many colloidal nano-catalysts with intrinsic lightweight bodies are usually suspended in the solution after the degradation reaction. Thus, some additional tedious and complicated separation procedures (physical centrifuge or membrane filtration, etc.) are always required for removing the suspended nano-catalysts from water samples. In order to overcome this obstacle, we prepared an ingeniously flexible PTC membrane via the resultant $\text{g-C}_3\text{N}_4/\text{h-BN}/\text{Au}$ NPs grafted into 3D porous supports, which can be conveniently extracted from the solution after the degradation reaction. Initially, some low-cost 3D bio-carbon frames were prepared by thermal treatment of natural loofah plants (Fig. 10 (a)), offering stable cross-linked porous microstructures for supporting the flexible PTC membranes. Moreover, the viscous bacterial nanocelluloses (BNCs, Fig. 10(b)) were then adopted in this work, enabling the colloidal $\text{g-C}_3\text{N}_4/\text{h-BN}/\text{Au}$ NPs (Fig. 10(c)) to be firmly immobilized into 3D bio-carbon frames. Therefore, the black-colored flexible PTC membrane (Fig. 10(d)) produced by the uniform mixture of the above three components can be readily tailored into any designated macro-shapes. For instance, the disc-shaped PTC membranes with diameters in the wide range of 2–16 cm (Fig. 10(e-f)) were conveniently established for meeting the practical degradation of wastewater systems with different volumes.

In order to verify the practical applicability of the resultant $\text{g-C}_3\text{N}_4/$

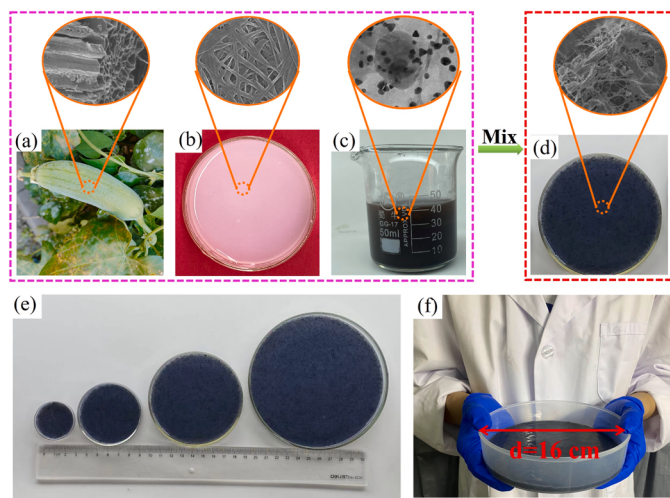


Fig. 10. (a-c) The 3D bio-carbon frames prepared by thermal treatment of natural loofah plants at 400 °C for 2 h, and viscous BNCs as well as the newly generated g-C₃N₄/h-BN/Au NPs. (d) the fabricated large-scale flexible PTC membrane with a diameter of about 5 cm, based on the mentioned three components. (e-f) The photograph images of the obtained flexible PTC membranes with different scales of 2–16 cm.

h-BN/Au NPs, the obtained flexible PTC membrane was further used for practical degradations of R6G pollutants in the actual water sample that was randomly collected from a no-name river in our surrounding environment (Fig. 11). Initially, each water sample was carefully filtrated with filter paper in order to remove large-grained slurries in the solution. The pH value of the water sample was then examined at about 5.8, confirming the weak acidic condition in this work. Then, we artificially added R6G dyes into the as-prepared water sample, offering 10 mg/L, 5 L mixed solution with orange-red color. The PTC membrane would be self-floated on the liquid surface after dropping into the R6G solution (Fig. 11), due to its large-surface areas and porous bio-carbon structures. In this way, the self-floating PTC membrane at the top of the solution has a greater ability to harvest more photon energy of natural solar light (solar spectra in Fig. S23(a)) in comparison with the target suspended in the middle or deposited at the bottom region. The power variation of solar light at the selected 2 h time region confirms that the incident optical energy was nearly fixed at ~1 kW/m² for each PTC degradation

test (Fig. S23(b)). After solar light irradiation of 2 h, it can be seen that the orange-red color of the R6G solution becomes colorless and then transparent (Fig. 11), implying the high-performance PTC degradation in the presence of the self-floating PTC membrane. Moreover, the degradation efficiency of the water sample before and after the PTC reaction was further examined by absorption spectra (Fig. 11). Besides the characteristic peak of R6G molecules at about 520 nm, some other weak absorption peaks located in the region of 200–300 nm were also detected on the pristine actual water sample, implying the co-existence of some concomitant human acids in the real-world scenarios that have been verified in our previous work [8]. By solar light irradiation of the self-floating PTC membrane, the characteristic peak of R6G molecules significantly drops from ~1.4 a.u at the initial state to ~0.01 a.u after the degradation reaction, supporting 99.5% organic pollutants can be eliminated from the solution. Meanwhile, the concomitant human acids would be also removed from the actual water sample since the corresponding absorption peaks in the range of 200–300 nm simultaneously disappeared after the PTC degradation. It reveals the excellent universality and versatility of the prepared flexible PTC membrane. Furthermore, the basic parameters of the actual water sample before and after PTC degradation were then illustrated in this work (Fig. S24), supporting the highly-efficient wastewater purification through solar light-triggered PTC reaction. Most importantly, the hybrid 3D porous microstructures of the self-floating flexible membrane were well maintained after one PTC reaction (Fig. 11), which can be easily extracted from the solution and then reused for the next recycling degradation. Then, we carried out the continuous 10 repeated degradation tests of actual water samples in this work, in order to verify the reusability of the obtained flexible PTC membrane. As expected, the acceptable deactivation of PTC degradation efficiency with about 2.2% lower than the pristine one can undoubtedly confirm the excellent long-term recyclability of the attractive PTC membrane. Thus, the self-floating and flexible PTC membrane with admirable degradation performances shows its great potential for promoting wastewater decontamination.

4. Conclusions

In summary, the extraordinary PTC nano-catalysts with ultrahigh activity and unprecedented thermostability at solar-activated heating condition have been developed by hybridizing polymeric g-C₃N₄ nanoplates with antioxidative h-BN nanosheets and then grafting with stable Au NPs. The smart g-C₃N₄/h-BN/Au NPs have been confirmed to possess

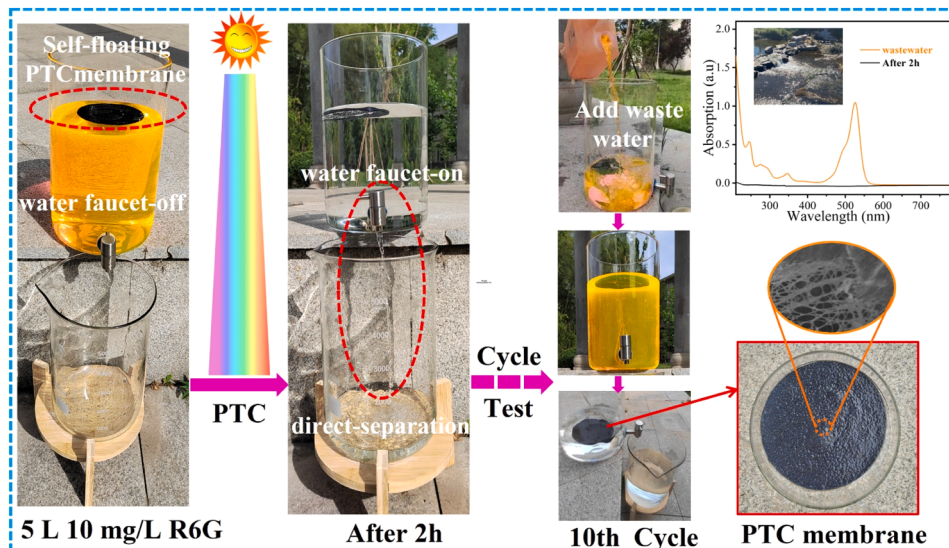


Fig. 11. Based on the prepared flexible PTC membrane, the practical elimination of organic R6G pollutants (10 mg/L, 5 L) in the actual real-world water samples. Each test was performed under natural solar light irradiation.

dual charge carrier transfer channels for simultaneously and separately migrating of broadband light-generated electrons and holes from the dominant g-C₃N₄ components to plasmonic Au NPs and electronegative h-BN insulators. Based on the resultant g-C₃N₄/h-BN/Au NPs, the optimal PTC degradation rate is achieved as high as about 0.30 min⁻¹ at solar light-driven high temperature (60 °C) condition, exceeding many previous nano-catalysts. The enhanced PTC activity is not only attributed to the making full use of photoexcited energetic electrons and holes but also ascribed to the highly-efficient reutilization of solar light-driven thermal energy. More importantly, the exceptional PTC recyclability can be also convincingly manifested on the resultant hybrid nano-architectures since the remaining ~99.8% degradation efficiency would be well maintained after consecutive 10 repeated tests within 500 min at solar-heated high temperature condition. The unparalleled thermostability is related to the remarkably inhibited photocorrosion of unstable g-C₃N₄ semiconductors. The efficient transmission of photo-excited holes can effectively reduce the serious accumulation of photoinduced oxidative species on the g-C₃N₄ semiconductors and then suppress possible self-oxidative decomposition of nitrogen anions to N₂. Finally, an ingenious self-floating PTC membrane has been obtained by uniformly mixing 3D bio-carbon frames and viscous BNCs as well as the resultant g-C₃N₄/h-BN/Au NPs. The established flexible PTC membrane was then practically applied to the recyclable degradations of organic pollutants in the actual water samples. Therefore, the present work is anticipated to provide an attractive and robust PTC nano-catalyst for propelling practical wastewater purification in the near future.

CRediT authorship contribution statement

Chang Wang: Methodology, Data curation, Formal analysis, Investigation, Writing – original draft. **Shihao Zhou:** Methodology, Data curation, Investigation. **Qingqiang Cui:** Data curation, Investigation. **Mengya Zhang:** Data curation, Investigation. **Linqi Zheng:** Data curation, Investigation. **Shuang Li:** Supervision, Writing – review & editing, Funding acquisition. **Xiangdong Liu:** Supervision, Writing – review & editing. **Ming Chen:** Supervision, Conceptualization, Writing – review & editing, Funding acquisition.

Declaration of Competing Interest

The authors declare that they have no known competing financial interests or personal relationships that could have appeared to influence the work reported in this paper.

Data Availability

Data will be made available on request.

Acknowledgments

This work was financially supported by the National Natural Science Foundation of China (NSFC) (Nos. 11905115, 12175126 and 11575102).

Appendix A. Supporting information

Supplementary data associated with this article can be found in the online version at [doi:10.1016/j.apcatb.2023.123491](https://doi.org/10.1016/j.apcatb.2023.123491).

References

- [1] S. Lotfi, K. Fischer, A. Schulze, A. Schäfer, Photocatalytic degradation of steroid hormone micropollutants by TiO₂-coated polyethersulfone membranes in a continuous flow-through process, *Nat. Nanotechnol.* 17 (2018) 417–423.
- [2] V. Parvulescu, F. Epron, H. Garcia, P. Granger, Recent progress and prospects in catalytic water treatment, *Chem. Rev.* 122 (2022) 2981–3121.
- [3] M. Sayed, J.G. Yu, G. Liu, M. Jaroniec, Non-noble plasmonic metal-based photocatalysts, *Chem. Rev.* 122 (2022) 10484–10537.
- [4] S.Y. Dong, Y.L. Zhao, J.Y. Yang, X.D. Liu, W. Li, L.Y. Zhang, Y.H. Wu, J.H. Sun, J. L. Feng, Y.F. Zhu, Visible-light responsive PDI/rGO composite film for the photothermal catalytic degradation of antibiotic wastewater and interfacial water evaporation, *Appl. Catal. B-Environ.* 291 (2021), 120127.
- [5] S.S. Lu, F.L. Liu, P.X. Qiu, M. Qiao, Y.F. Li, Z.W. Cheng, N.X. Xue, X.K. Hou, C. M. Xu, Y.B. Xiang, F.P. Peng, Z.B. Guo, Photothermal-assisted photocatalytic degradation with ultrahigh solar utilization: Towards practical application, *Chem. Eng. J.* 379 (2020), 122382.
- [6] E.Z. Lin, R. Huang, J. Wu, Z.H. Kang, K.H. Ke, N. Qin, D.H. Bao, Recyclable CoFe₂O₄ modified BiOCl hierarchical microspheres utilizing photo, photothermal and mechanical energy for organic pollutant degradation, *Nano Energy* 89 (2021), 106403.
- [7] X.J. Lang, J.C. Zhao, X.D. Chen, Cooperative photoredox catalysis, *Chem. Soc. Rev.* 45 (2016) 3026.
- [8] C. Wang, H. Ma, Y. Tian, A.X. Jiao, M.Y. Zhang, L.Q. Zheng, S. Li, M. Chen, Polymeric layered semiconductor-supported black nano-sandwiches with synergistic photo-thermal catalysis for efficient wastewater decontamination, *Chem. Eng. J.* 446 (2022), 136977.
- [9] L.Q. Jing, M. Xie, Y.G. Xu, C. Tong, H. Zhao, N. Zhong, H.M. Li, I. Gates, J.G. Hu, Multifunctional 3D MoS_x/Zn₃In₂S₆ nanoflower for selective photothermal-catalytic biomass oxidative and non-selective organic pollutants degradation, *Appl. Catal. B-Environ.* 318 (2022), 121814..
- [10] M.Q. Yang, C.F. Tan, W.H. Lu, K.Y. Zeng, G.W. Ho, Spectrum tailored defective 2D semiconductor nanosheets aerogel for full-spectrum-driven photothermal water evaporation and photochemical degradation, *Adv. Funct. Mater.* 30 (2020), 2004460.
- [11] Z.X. Gan, X.L. Wu, M. Meng, X.B. Zhu, L. Yang, P. Chu, Photothermal contribution to enhanced photocatalytic performance of graphene-based nanocomposites, *ACS Nano* 8 (2014) 9304–9310.
- [12] Y.D. Zhao, J.Y. Han, Y.T. Chen, Y. Su, Y.M. Cao, B. Wu, S.M. Yu, M.D. Li, Z. S. Wang, M. Zheng, M.P. Zhuo, L.S. Liao, Organic charge-transfer cocrystals toward large-area nanofiber membrane for photothermal conversion and imaging, *ACS Nano* 16 (2022) 15000–15007.
- [13] Z.L. Wang, Y.Y. Wang, Y.N. Zhang, X. Sun, Y. Lou, Y. Zhang, Y.M. Dong, C.S. Pan, Y.F. Zhu, Efficient photothermal degradation on Bi₁₂CoO₂₀ sillenite with a strong internal electric field induced by the thermal effect, *Appl. Catal. B-Environ.* 313 (2022), 121452..
- [14] B. Wang, M.Y. Qi, C. Han, Z.R. Tang, Y.J. Xu, Photocorrosion inhibition of semiconductor-based photocatalysts: basic principle, current development, and future perspective, *ACS Catal.* 9 (2019) 4642–4687.
- [15] S. Chen, D.L. Huang, P. Xu, W.J. Xue, L. Lei, M. Cheng, R.Z. Wang, X.G. Liu, R. Deng, Semiconductor-based photocatalysts for photocatalytic and photoelectrochemical water splitting: will we stop with photocorrosion? *J. Mater. Chem. A* 8 (2020) 2286.
- [16] Y.B. Kuang, Q.X. Jia, G.J. Ma, T. Hisatomi, T. Minegishi, H. Nishiyama, M. Nakabayashi, N. Shibata, T. Yamada, A. Kudo, K. Domen, Ultrastable low-bias water splitting photoanodes via photocorrosion inhibition and in situ catalyst regeneration, *Nat. Energy* 2 (2016), 16191.
- [17] F.S. Guo, S.R. Li, C. Yang, J.S. Zhang, Y.D. Hou, X.C. Wang, A highly crystallized hexagonal BCN photocatalyst with superior anticorrosion properties, *Adv. Opt. Mater.* 10 (2022), 2200282.
- [18] H.C. Yu, H.X. Kang, Z.B. Jiao, G.X. Lü, Y.P. Bi, Tunable photocatalytic selectivity and stability of Ba-doped Ag₃PO₄ hollow nanosheets, *Chin. J. Catal.* 36 (2015) 1587–1595.
- [19] T. Cai, L.L. Wang, Y.T. Liu, S.Q. Zhang, W.Y. Dong, H. Chen, X.Y. Yi, J.L. Yuan, X. N. Xia, C.B. Liu, S.L. Luo, Ag₃PO₄/Ti₃C₂ MXene interface materials as a Schottky catalyst with enhanced photocatalytic activities and anti-photocorrosion performance, *Appl. Catal. B-Environ.* 239 (2018) 545–554.
- [20] L.Z. Sun, W.J. Wang, C. Zhang, M. Cheng, Y. Zhou, Y. Yang, H.Z. Luo, D.Y. Qin, C. Huang, Z.L. Ouyang, Multiple optimization strategies for improving photocatalytic performance of the h-BN/flower-ring g-C₃N₄ heterostructures: Morphology engineering and internal electric field effect, *Chem. Eng. J.* 446 (2022), 137027.
- [21] Z.Z. Zhang, M.Y. Wang, Z.X. Chi, W.J. Li, H. Yu, N. Yang, H.B. Yu, Internal electric field engineering step-scheme-based heterojunction using lead-free Cs₂Bi₂Br₉ perovskite-modified In₄SnS₆ for selective photocatalytic CO₂ reduction to CO, *Appl. Catal. B-Environ.* 313 (2022), 121426.
- [22] S. Mondal, L. Sahoo, C.P. Vinod, U. Gautam, Facile transfer of excited electrons in Au/SnS₂ nanosheets for efficient solar-driven selective organic transformations, *Appl. Catal. B-Environ.* 286 (2021), 119927.
- [23] Y.O. Wang, R. Godin, J. Durrant, J.W. Tang, Efficient hole trapping in carbon dot/oxygen-modified carbon nitride heterojunction photocatalysts for enhanced methanol production from CO₂ under neutral conditions, *Angew. Chem. Int. Ed.* 60 (2021) 20811–20816.
- [24] F.L. Wang, Y.F. Wang, Y.P. Feng, Y.Q. Zeng, Z.J. Xie, Q.X. Zhang, Y.H. Su, P. Chen, Y. Liu, K. Yao, W.Y. Lv, G.G. Liu, Novel ternary photocatalyst of single atom-dispersed silver and carbon quantum dots co-loaded with ultrathin g-C₃N₄ for broad spectrum photocatalytic degradation of naproxen, *Appl. Catal. B-Environ.* 221 (2018) 510–520.
- [25] H.B. Fu, T.G. Xu, S.B. Zhu, Y.F. Zhu, Photocorrosion Inhibition and Enhancement of Photocatalytic Activity for ZnO via Hybridization with C₆₀, *Environ. Sci. Technol.* 42 (2008) 8064–8069.
- [26] D. Mateo, J.L. Cerrillo, S. Durini, J. Gascon, Fundamentals and applications of photo-thermal catalysis, *Chem. Soc. Rev.* 50 (2021) 2173.

[27] H.C. Zhang, P.C. Guo, X. Zhang, G.P. Sheng, Developing a solar photothermal method for peroxydisulfate activation for water purification: Taking degradation of sulfamethoxazole as an example, *Chem. Eng. J.* 403 (2021), 126324.

[28] J. Ma, H.Y. Li, L.P. Chi, H.K. Chen, C.Z. Chen, Changes in activation energy and kinetics of heat-activated persulfate oxidation of phenol in response to changes in pH and temperature, *Chemosphere* 189 (2017) 86–93.

[29] R.G. Li, H.X. Han, F.X. Zhang, D.G. Wang, C. Li, Highly efficient photocatalysts constructed by rational assembly of dual-cocatalysts separately on different facets of BiVO_4 , *Energy Environ. Sci.* 7 (4) (2014) 1369–1376.

[30] C. Peng, P. Wei, X.Y. Li, Y.P. Liu, Y.H. Cao, H.J. Wang, H. Yu, F. Peng, L.Y. Zhang, B. Zhang, K.L. Lv, High efficiency photocatalytic hydrogen production over ternary $\text{Cu}/\text{TiO}_2/\text{Ti}_3\text{C}_2\text{T}_x$ enabled by low-work-function 2D titanium carbide, *Nano Energy* 53 (2018) 97–107.

[31] Q.J. Xiang, J.G. Yu, M. Jaroniec, Synergistic effect of MoS_2 and graphene as cocatalysts for enhanced photocatalytic H_2 production activity of TiO_2 nanoparticles, *J. Am. Chem. Soc.* 134 (15) (2012) 6575–6578.

[32] Y.S. Xie, L. Yuan, N. Zhang, Y.J. Xu, Light-tuned switching of charge transfer channel for simultaneously boosted photoactivity and stability, *Appl. Catal. B-Environ.* 238 (2018) 19–26.

[33] X.D. Wan, Y.Y. Gao, M. Eshete, M. Hu, R.R. Pan, H.Z. Wang, L.Z. Liu, J. Liu, J. Jiang, S. Brovelli, J. Zhang, Simultaneous harnessing of hot electrons and hot holes achieved via n-metal-p Janus plasmonic heteronano-crystals, *Nano Energy* 98 (2022), 107217.

[34] C.B. Bie, B.C. Zhu, L.X. Wang, H. Yu, C.H. Jiang, T. Chen, J.G. Yu, A bifunctional $\text{CdS}/\text{MoO}_2/\text{MoS}_2$ catalyst enhances photocatalytic H_2 evolution and pyruvic acid synthesis, *Angew. Chem. Int. Ed.* 161 (44) (2022) 12045.

[35] G. Mamba, A.K. Mishra, Graphitic carbon nitride ($\text{g-C}_3\text{N}_4$) nanocomposites: a new and exciting generation of visible light driven photocatalysts for environmental pollution remediation, *Appl. Catal. B-Environ.* 198 (2016) 347–377.

[36] J.Z. Jiang, L. Ou-yang, L.H. Zhu, A.M. Zheng, J. Zou, X.F. Yi, H. Tang, Dependence of electronic structure of $\text{g-C}_3\text{N}_4$ on the layer number of its nanosheets: a study by Raman spectroscopy coupled with first-principles calculations, *Carbon* 80 (2014) 213–221.

[37] V. Jain, R.K. Kashyap, P.P. Pillai, Plasmonic photocatalysis: activating chemical bonds through light and plasmon, *Adv. Opt. Mater.* 10 (15) (2022), 2200463.

[38] Q.H. Weng, X.B. Wang, X. Wang, Y. Bando, D. Golberg, Functionalized hexagonal boron nitride nanomaterials: emerging properties and applications, *Chem. Soc. Rev.* 45 (14) (2016) 3989.

[39] Q.R. Cai, S. Mateti, W.R. Yang, R. Jones, K.J. Watanabe, T. Taniguchi, S.M. Huang, Y. Chen, L.H. Li, Boron nitride nanosheets improve sensitivity and reusability of surface-enhanced Raman spectroscopy, *Angew. Chem. Int. Ed.* 55 (29) (2016) 8405.

[40] G. Kim, M. Kim, C. Hyun, S. Hong, K.Y. Ma, H.S. Shin, H. Lim, Hexagonal boron nitride/Au substrate for manipulating surface plasmon and enhancing capability of surface-enhanced Raman spectroscopy, *ACS Nano* 10 (12) (2016) 11156–11162.

[41] M. Higashi, K. Domen, R. Abe, Highly stable water splitting on oxynitride TaON photoanode system under visible light irradiation, *J. Am. Chem. Soc.* 134 (16) (2012) 6968–6971.

[42] H. Fujio, H. Kunioku, D.C. Kato, H. Suzuki, M. Higashi, H. Kageyama, R. Abe, Layered perovskite oxychloride $\text{Bi}_4\text{NbO}_8\text{Cl}$: a stable visible light responsive photocatalyst for water splitting, *J. Am. Chem. Soc.* 138 (7) (2016) 2082–2085.

[43] R. Abe, M. Higashi, K. Domen, Facile fabrication of an efficient oxynitride TaON photoanode for overall water splitting into H_2 and O_2 under visible light irradiation, *J. Am. Chem. Soc.* 132 (34) (2010) 11828–11829.

[44] G. Kresse, D. Joubert, From ultrasoft pseudopotentials to the projector augmented-wave method, *Phys. Rev. B* 59 (3) (1999), 1758–177.

[45] J.P. Perdew, K. Burke, M. Ernzerhof, Generalized gradient approximation made simple, *Phys. Rev. Lett.* 77 (18) (1996) 3865–3868.

[46] C. Wang, S.H. Zhou, Y. Tian, A.X. Jiao, H. Ma, M.Y. Zhang, L.Q. Zheng, X.D. Liu, Q. Q. Cui, S. Li, M. Chen, Super-hydrophilic SERS sensor with both ultrahigh activity and exceptional 3D spatial uniformity for sensitive detection of toxic pollutants, *Appl. Surf. Sci.* 603 (2022), 154445.

[47] A.X. Jiao, Q.Q. Cui, S. Li, H.S. Li, L.L. Xu, Y. Tian, H. Ma, M.Y. Zhang, X.D. Liu, M. Chen, Aligned TiO_2 nanorod arrays decorated with closely interconnected Au/Ag nanoparticles: Near-infrared SERS active sensor for monitoring of antibiotic molecules in water, *Sens. Actuators, B* 350 (2022), 130848.

[48] Y. Tian, Q.Q. Cui, L.L. Xu, A.X. Jiao, H. Ma, C. Wang, M.Y. Zhang, X.L. Wang, S. Li, M. Chen, Alloyed AuPt nanoframes loaded on h-BN nanosheets as an ingenious ultrasensitive near-infrared photoelectrochemical biosensor for accurate monitoring glucose in human tears, *Biosens. Bioelectron.* 192 (2021), 113490.

[49] A.X. Jiao, Q.Q. Cui, S. Li, Y. Tian, H. Ma, C. Wang, M.Y. Zhang, M. Chen, G.H. Li, X. D. Liu, Double profound enhancements of Cu_2O nano-octahedrons connected by intertwined Ag nanovines for elevating SERS activity toward ultrasensitive pesticide detection, *Opt. Express* 30 (1) (2022) 588–602.

[50] H. Zhang, L.L. Xu, Y. Tian, A.X. Jiao, S. Li, X.D. Liu, M. Chen, F. Chen, Convenient synthesis of 3D fluffy PtPd nanocarbons loaded on 2D h-BN supports as highly efficient and stable electrocatalysts for alcohol oxidation reaction, *ACS Omega* 4 (6) (2019) 11163–11172.

[51] I. Papaillas, T. Giannakopoulou, N. Todorova, D. Demotikali, T. Vaimakis, C. Trapalis, Effect of processing temperature on structure and photocatalytic properties of $\text{g-C}_3\text{N}_4$, *Appl. Surf. Sci.* 358 (2015) 278–286.

[52] D.S. Wang, H.T. Sun, Q.Z. Luo, X.L. Yang, R. Yin, An efficient visible-light photocatalyst prepared from $\text{g-C}_3\text{N}_4$ and polyvinyl chloride, *Appl. Catal. B-Environ.* 156–157 (2014) 323–330.

[53] H. Ma, Y. Tian, A.X. Jiao, C. Wang, M.Y. Zhang, L.Q. Zheng, G.H. Li, S. Li, M. Chen, Extraordinary approach to further boost plasmonic NIR-SERS by cryogenic temperature-suppressed non-radiative recombination, *Opt. Lett.* 47 (3) (2022) 670–673.

[54] S. Ben-Jaber, W.J. Peveler, R. Quesada-Cabrera, E. Cortes, C. Sotelo-Vazquez, N. Abdul-Karim, S.A. Maier, I.P. Parkin, Photo-induced enhanced Raman spectroscopy for universal ultra-trace detection of explosives, pollutants and biomolecules, *Nat. Commun.* 7 (2016) 12189.

[55] J. Lin, J. Yu, O.U. Akakuru, X.T. Wang, B. Yuan, T.X. Chen, L. Guo, A.G. Wu, Low temperature-boosted high efficiency photo-induced charge transfer for remarkable SERS activity of ZnO nanosheets, *Chem. Sci.* 11 (35) (2020) 9414–9420.

[56] M.Y. Zhang, Y. Tian, A.X. Jiao, H. Ma, C. Wang, L.Q. Zheng, S. Li, M. Chen, Synergistic double laser beam-boosted liquid-NIR-SERS for ultralow detection of non-adsorptive polycyclic aromatic hydrocarbons in lake water, *Nanophotonics* 11 (12) (2022) 2875–2889.

[57] R. Shi, Y.H. Cao, Y.J. Bao, Y.F. Zhao, Geoffrey I.N. Waterhouse, Z.Y. Fang, L.Z. Wu, C.H. Tung, Y.D. Yin, T.R. Zhang, Self-Assembled Au/CdSe Nanocrystal Clusters for Plasmon-Mediated Photocatalytic Hydrogen Evolution, *Adv. Mater.* 29 (2017), 1700803.

[58] H.J. Yu, Y.F. Zhao, C. Zhou, L. Shang, Y. Peng, Y.H. Cao, L.Z. Wu, C.H. Tung, T. R. Zhang, Carbon quantum dots/ TiO_2 composites for efficient photocatalytic hydrogen evolution, *J. Mater. Chem. A* 2 (2014) 3344.

[59] X.J. Bai, R.L. Zong, C.X. Li, D. Liu, Y.F. Liu, Y.F. Zhu, Enhancement of visible photocatalytic activity via $\text{Ag}/\text{C}_3\text{N}_4$ core-shell plasmonic composite, *Appl. Catal. B-Environ.* 147 (2014) 82–91.

[60] L.L. Xu, Q.Q. Cui, H. Zhang, A.X. Jiao, Y. Tian, S. Li, H.S. Li, M. Chen, F. Chen, Ultra-clean PtPd nanoflowers loaded on GO supports with enhanced low-temperature electrocatalytic activity for fuel cells in harsh environment, *Appl. Surf. Sci.* 511 (2020), 145603.

[61] F.F. Ren, H.W. Wang, C.Y. Zhai, M.S. Zhu, R.R. Yue, Y.K. Du, P. Yang, J.K. Xu, W. S. Lu, Clean method for the synthesis of reduced graphene oxide-supported PtPd alloys with high electrocatalytic activity for ethanol oxidation in alkaline medium, *ACS Appl. Mater. Interfaces* 6 (5) (2014) 3607–3614.

[62] Y.R. Tian, X.T. Li, F.Y. Wang, C.J. Gu, Z.Q. Zhao, H.J. Si, T. Jiang, SERS-based immunoassay and degradation of CA19-9 mediated by gold nanowires anchored magnetic-semiconductor nanocomposites, *J. Hazard. Mater.* 403 (2021), 124009.

[63] W. Liu, W. Hu, Green fabrication of h-BN/ $\text{g-C}_3\text{N}_4$ with efficient holes transfer towards highly improved photocatalytic CO_2 reduction and RhB degradation, *Mater. Charact.* 191 (2022), 112165.

[64] L. Xu, J. Zeng, Q. Li, L.B. Xia, X. Luo, Z.L. Ma, B.J. Peng, S.X. Xiong, Z.Q. Li, L. Wang, Y.P. Lei, Defect-engineered 2D/2D hBN/ $\text{g-C}_3\text{N}_4$ Z-scheme heterojunctions with full visible-light absorption: Efficient metal-free photocatalysts for hydrogen evolution, *Appl. Surf. Sci.* 547 (2021), 149207.

[65] L.B. Jiang, X.Z. Yuan, G.M. Zeng, Z.B. Wu, J. Liang, X.H. Chen, L.J. Leng, H. Wang, H. Wang, Metal-free efficient photocatalyst for stable visible-light photocatalytic degradation of refractory pollutant, *Appl. Catal. B-Environ.* 221 (2018) 715–725.

[66] D. Tu, H.W. Liao, Q.L. Deng, Synthesis of BN/ $\text{g-C}_3\text{N}_4$ as visible-light-driven photocatalysts for degradation of different organic pollutants, *Chem. Sel.* 3 (25) (2018) 7170–7177.

[67] J.K. Ren, P. Innocenzi, 2D boron nitride heterostructures: recent advances and future challenges, *Small Struct.* 2 (11) (2021), 2100068.